A mathematical model for direct ethanol fuel cells based on detailed ethanol electro-oxidation kinetics

Article *in* Applied Energy · May 2019

DOI: 10.1016/j.apenergy.2019.05.067

CITATIONS
0

READS
81

3 authors:

Juan Sánchez-Monreal
German Aerospace Center (DLR)
13 PUBLICATIONS **11** CITATIONS

SEE PROFILE

Pablo Angel Garcia-Salaberri
University Carlos III de Madrid
67 PUBLICATIONS **220** CITATIONS

SEE PROFILE

Marcos Vera
University Carlos III de Madrid
101 PUBLICATIONS **550** CITATIONS

SEE PROFILE

A mathematical model for direct ethanol fuel cells based on detailed ethanol electro-oxidation kinetics

Juan Sánchez-Monreal[1], Pablo A. García-Salaberri[2], Marcos Vera[2,*]

[1] *Deutsches Zentrum für Luft und Raumfahrt (DLR),*

Institute of Engineering Thermodynamics, 70569 Stuttgart, Germany

[2] *Departamento de Ingeniería Térmica y de Fluidos, Universidad Carlos III de Madrid,*

28911 Leganés, Spain

Full-length article

Running Title: **A mathematical model for DEFCs based on detailed EOR kinetics**

Preprint submitted to *Applied Energy*

April 2, 2019

* Corresponding author: **Marcos Vera**

Departamento de Ingeniería Térmica y de Fluidos

Universidad Carlos III de Madrid

Avda. de la Universidad, 30

28911 Leganés, Spain

Email address: marcos.vera@uc3m.es

Pho: +34 91 624 9987, *Fax*: +34 91 624 9430

A mathematical model for direct ethanol fuel cells based on detailed ethanol electro-oxidation kinetics

Juan Sánchez-Monreal[a], Pablo A. García-Salaberri[b], Marcos Vera[b,*]

[a]*Deutsches Zentrum für Luft und Raumfahrt (DLR), Institute of Engineering Thermodynamics, 70569 Stuttgart, Germany*
[b]*Departamento de Ingeniería Térmica y de Fluidos, Universidad Carlos III de Madrid, 28911 Leganés, Spain*

Abstract

This paper presents an isothermal, single-phase model for direct ethanol fuel cells. The ethanol electro-oxidation reaction is described using a detailed kinetic model that is able to predict anode polarization and product selectivity data. The anode kinetic model is coupled to a one-dimensional (1D) description for mass and charge transport across the membrane electrode assembly, which accounts for the mixed potential induced in the cathode catalyst layer by the crossover of ethanol and acetaldehyde. A simple 1D advection model is used to describe the spatial variation of the concentrations of the different species as well as the output and parasitic current densities along the flow channels. The proposed 1D+1D model includes two adjustable parameters that are fitted by a genetic algorithm in order to reproduce previous experimental data. The calibrated model is then used to investigate the consumption of ethanol and the production, accumulation and consumption of acetaldehyde along the flow channels, which yields the product selectivity at different channel cross-sections. A parametric study is also presented for varying ethanol feed concentrations and flow rates. The results obtained under ethanol starvation conditions highlight the role of acetaldehyde as main free intermediate, which is first produced and later consumed once ethanol is fully depleted. The detailed kinetic description of the ethanol oxidation reaction enables the computation of the four efficiencies (i.e., theoretical, voltage, faradaic, end energy utilization) that characterize the operation of direct ethanol fuel cells, thus allowing to present overall fuel efficiency vs. cell current density curves for the first time.

Keywords: Direct ethanol PEM fuel cells, detailed EOR kinetics, modeling, product selectivity, faradic efficiency, energy utilization

*Corresponding author. Tel.: +34-916249987; fax: +34-916249430.
Email addresses: Juan.SanchezMonreal@dlr.de (Juan Sánchez-Monreal), pagsalab@ing.uc3m.es (Pablo A. García-Salaberri), marcos.vera@uc3m.es (Marcos Vera)
URL: http://fluidosuc3m.es/people/mvcoello (Marcos Vera)

1. Introduction

Fuel cells are electrochemical devices that convert the chemical energy contained in a fuel directly into electrical energy with high thermodynamic efficiency, low pollutant emissions, and essentially no moving parts [1]. Unlike low-temperature polymer electrolyte membrane (PEM) fuel cells, powered by hydrogen, direct alcohol fuel cells (DAFCs) use liquid alcohols as fuels, which avoids the need of a reforming step and facilitates the transport, storage and handling of the fuels through the existing distribution network [2]. In particular, DAFCs constitute a promising power source for portable electronic devices and small electric vehicles [3, 4].

Among alcohols, ethanol stands out as a very attractive fuel for sustainable energy systems. It presents multiple advantages over its main competitor (i.e., methanol) including its lower toxicity, production via fully renewable processes, and higher theoretical energy density [5]. Ethanol is currently obtained on a large scale from the conversion of sugars, biomass, cereals or other carbon-based feedstock [6], and can be easily and safely stored and transported with systems already established for the petrol station network [7]. More recently, ethanol has also attracted attention as a renewable fuel for the production of hydrogen in electrochemical reformers [8].

In contrast to its favorable thermodynamic performance compared to hydrogen [5], and its various advantages over other alcohols such as methanol, the kinetics of ethanol electro-oxidation is far more complex and therefore slower. It is characterized by an intricate reaction mechanism that involves multi-electron transfer and complex C-C bond cleavage [7]. In state-of-the-art direct ethanol fuel cells (DEFCs), the ethanol oxidation reaction (EOR) faces a central drawback related to the C-C bond cleavage step, which is critical for the activation of the so-called C_1 pathway leading to the complete oxidation of ethanol to CO_2 with the release of 12 electrons. Otherwise, the reaction path follows the C_2 pathway, where the C-C bond remains intact, resulting in the incomplete oxidation of ethanol to acetaldehyde and acetic acid, with the release of only 2 and 4 electrons, respectively [9, 10].

Besides i) the low CO_2 selectivity that characterizes most state-of-the-art electrocatalysts [11], additional drawbacks of DEFC technology include ii) the low activity of those catalysts, which only improves at high temperatures, iii) the cross-over of ethanol and other reactive species through Nafion® type membranes, which reduces fuel utilization, iv) the significant depolarization of the cathode electrode resulting from the parasitic oxidation of the species crossing the membrane, and iv) the poisoning of the anode and cathode electrodes by strongly adsorbed intermediates (such as CO) formed during the direct and parasitic oxidation of ethanol and acetaldehyde [7].

The combined effect of these technical problems is to significantly reduce the energy efficiency of

the system. The overall efficiency of a DEFC is determined by the product of the theoretical efficiency ($\epsilon_{rev} = \Delta G/\Delta H \simeq 0.97$), the voltage efficiency ($\epsilon_E = E_{cell}/E_{rev}$, where $E_{rev} \simeq 1.4$ V is the reversible cell potential), the faradaic efficiency ($\epsilon_F = n_{eff}/12$, where n_{eff} is the average number of electrons obtained per ethanol molecule, and the energy utilization ($\epsilon_U = \Delta H/(\Delta H + \Delta H_{loss})$, where ΔH is the available enthalpy actually used to produce current and ΔH_{loss} is the enthalpy loss due to crossover), namely

$$\epsilon_T = \epsilon_{rev} \times \epsilon_E \times \epsilon_F \times \epsilon_U \tag{1}$$

The theoretical or thermodynamic efficiency, ϵ_{rev}, is fixed, and corresponds to the complete oxidation of ethanol to CO_2. The voltage efficiency, ϵ_E, is due to the different overpotentials that appear in the cell (i.e., activation and ohmic overpotentials), and is lower in DEFCs compared to other low-temperature PEM fuel cells due to the combination of the low catalyst activity, electrode poisoning and cathode depolarization due to crossover. The energy utilization factor is induced by species crossover, an effect that is particularly relevant at low current densities and high ethanol concentrations. Due to the dual role of acetaldehyde, which may act both as product or as reactant, in DEFCs it is more convenient to consider the energy utilization factor than the classical fuel utilization customarily used in direct methanol fuel cells (DMFCs). This is because, unlike methanol in DMFCs, a significant fraction of the ethanol feed to the cell is only partially oxidized to acetaldehyde, which still has the potential to release a significant amount of energy under appropriate conditions. Thus, accounting only for the ethanol used in the anode and lost to the cathode would disregard the important role played by acetaldehyde in DEFCs, to be discussed below.

However, the real Achilles' heel of DEFCs is their low faradaic efficiency, ϵ_F, which poses the most serious challenge for the future development of this technology. While in fuel cells based on simpler fuels, such as hydrogen or ethanol, complete oxidation is easily achieved leading to near-unity faradaic efficiencies, in DEFCs the faradaic efficiency is much smaller due to the low CO_2 selectivity of currently available catalysts. This results in the production of partially oxidized products such as acetaldehyde or acetic acid, instead of the complete oxidation of ethanol to CO_2. The role of the faradaic efficiency in the evaluation of DEFCs energy-conversion performance has long been recognized in the literature [12, 13]. However, research on this topic has been mostly devoted to the experimental assessment of the selectivity towards CO_2 of different catalysts formulations and supports [14]. The most thorough investigation of the faradaic efficiency of ethanol electro-oxidation has been carried out by Pickup et al. [15, 16]. In a long series of papers, Pickup's group has developed or applied a large variety of experimental techniques (operating DEFCs in crossover mode [17], using the flow rate dependence of the current to estimate the faradaic efficiency of ethanol oxidation [16, 18], pulsing the potential or current to increase CO_2

yields [19, 20, 21], applying different methodologies for the online analysis of DEFC products [22, 23], etc.) combined with simple but insightful experiment-based models [16, 24], to analyze systematically both PEM electrolysis cells and DEFCs. These techniques have enabled the determination of the stoichiometry, efficiency, and product distribution for ethanol electrolysis or electro-oxidation in fuel cell hardware under different operating conditions [25], employing different catalysts formulations [26] and structures [24, 27, 28, 29], and for different system or electrode architectures [30, 31]. Not to mention the precise assessment of the effects of species crossover [32].

In this context, more thorough mathematical models would serve as a powerful tool to analyze the complex physicochemical interactions between the electrochemical reactions and the mass and charge transport phenomena that take place in DEFCs. Advanced multi-scale and multi-physics models have enabled significant improvements in fuel cell design, operation and performance in more mature fuel cell technologies, such as PEMFCs [33, 34, 35, 36, 37] and DMFCs [38, 39, 40]. Some of them couple traditional continuous macro-homogeneous descriptions with pore-network models [41, 42] or lattice Boltzman simulations [43] for solving the pore scale, take into account inhomogeneous compression effects [44], or are validated against time-resolved neutron imaging data [45]. By contrast, a survey of the available models for DEFCs [46], which are briefly reviewed below, shows that these models are still in their early stages and are not yet able to fully describe the operation of a DEFC system as a whole. They exclude systematically, for instance, the prediction of the faradaic efficiency of the cell, or the evaluation of the energy utilization factor.

The first DEFC models considered that the EOR was much slower than the oxygen reduction reaction (ORR). As a result, the activation overpotential of the cathodic reaction was often neglected [47, 48]. Later work modeled the ORR as a single Tafel reaction [49, 50, 51, 52, 53], while more recent models included also the reverse reaction using Butler-Volmer kinetics [54]. Most early DEFC models also assumed the complete oxidation of ethanol to CO_2 with the transfer of 12 electrons [47, 48, 49, 50, 53]. Surprisingly, this drastic simplification, which completely overlooks the electrochemical complexities of the EOR, is still used today [55, 56]. By contrast, other models considered the oxidation of ethanol to acetic acid with the transfer of only 4 electrons [52, 57, 58, 59, 60, 61, 62, 63, 64]. It was not until recently that some DEFC models started to account for the complex multi-step kinetics of the EOR, including the effect of intermediate species such as acetic acid and acetaldehyde [54, 65, 66]. These models typically involved the calculation of the coverage factors of the adsorbed intermediates, an approach that had been previously applied to DMFC modeling [67, 68].

Due to the relevance of crossover in DEFC performance, most models also include this effect [47, 48,

49, 50, 55, 56, 58, 62, 63, 64]. Since the molecular structures of ethanol and methanol are very similar, all crossover models for ethanol are based on those previously developed for methanol, where the crossover fluxes are driven mainly by diffusion and electro-osmotic drag, with hydraulic permeation only included occasionally [53]. The crossover of other free intermediate species, such as acetaldehyde or acetic acid, or even the crossover of oxygen from cathode to anode, have only been modeled in a limited number of works [54, 65, 66].

A common feature of most DEFC models published to date is that they are limited to one-dimensional (1D) across-the-channel formulations [47, 48, 49, 50, 52, 53, 54, 57]. In this case, species transport across the MEA is driven by molecular diffusion [54, 57], or by the combined action of molecular diffusion and water drag [47, 48, 49, 50, 52, 53]. Due to the key role played by the electrochemical reactions, the catalyst layers are often represented as porous media of finite thickness with non-uniform species concentrations [47, 48, 49, 50, 52, 53, 54]. Two-dimensional (2D) along-the-channel models are more scarce [51, 61, 65] and typically treat the electrochemical reactions at the catalyst layers as boundary, or jump, conditions. Fully three-dimensional (3D) studies have also been reported, but are still limited to very simple geometries [62, 63, 64] or to CFD analyses of realistic flow fields that ignore all electrochemical phenomena [69]. It is worth noting that all modeling studies except one [56] have considered isothermal conditions. This is because the reported temperature differences across the MEA are of the order of tenths of a degree [56], which is consistent with the low electrochemical activity of passive DEFCs [70].

A particularly illuminating investigation for the development of this work has been the model of Meyer et al. [54], who proposed a branched reaction mechanism for the EOR that involved different electron transfers depending on the pathway. Despite its good agreement in terms of polarization curves, the composition of the product mixture predicted by Meyer's model was far from satisfactory [71]. To overcome this problem, an improved kinetic model was recently proposed by the authors [66], including a new chemical pathway for ethanol oxidation that had not been previously considered by Meyer et al. [54]. The improved model showed greater adaptability, via genetic algorithm optimization, to different binary Pt-based catalyst compositions, and was able to reproduce both anode overpotential and product selectivity data in a wide range of operation conditions. Considering different free intermediate species also enabled an improved modeling of the crossover fluxes and the resulting cathode mixed potential.

The above review of currently available DEFC models clearly shows that there is still room for more innovative models in order to address the critical issues that stand in the way of this technology. This will surely help to bridge the gap between fundamental research and implementation of future generation DAFCs. In particular, to the best of our knowledge, there is still no DEFC model able to predict the effect

of design and operational parameters both on the voltage efficiency, the faradaic efficiency and the fuel utilization, for both high and low ethanol stoichiometry conditions. To achieve this goal, the proposed model should demonstrate its ability to reproduce experimental results corresponding to anode, cathode and cell polarization data separately, as well as to predict the product selectivity of the cell, thereby enabling the computation of the faradaic efficiency, and from it the overall fuel cell efficiency. The aim of this paper is to report a first attempt aiming to fulfill these requirements. To the authors knowledge, the mathematical model to be presented below is one of the most advanced DEFCs models currently available in the literature. It presents a comprehensive description of electrochemistry and transport processes in this type of fuel cells, and could be very useful to interpret experimental data and to identify critical issues in the design and operation of next generation DEFCs.

2. Model assumptions and physical domain

This paper presents an isothermal single-phase 1D+1D model for liquid-feed DEFCs involving free and adsorbed intermediate species. Figure 1 shows a schematic representation of the modeling domain, showing the coordinate system and the different regions of the cell. The assumptions adopted in the development of the mathematical model are: *i*) the cell operates in steady-state; *ii*) the cell temperature (T) is uniform; *iii*) the concentrations of the free species (ethanol, acethaldehyde, acetic acid, and CO_2) are sufficiently small for the liquid phase to be considered a diluted aqueous solution; *iv*) the membrane (Nafion® 117) is fully hydrated and is impermeable to gases; *v*) the overpotentials, coverage factors, and concentrations of the free species are uniform across the catalyst layers; *vi*) the anode catalyst layer consists of a Pt-based binary catalyst that allows the absorption of hydroxyl groups at lower potentials on the secondary metal according to the bifunctional mechanism described in [12, 72, 73]; and *vii*) the only species that permeate trough the membrane are ethanol and acetaldehyde, which are completely oxidized to acetic acid at the cathode catalyst layer.

The model incorporates two adjustable parameters: *i)* an effective electronic/contact resistance, R_{cont}, which contributes to the cell ohmic resistance in addition to the protonic resistance of the membrane, and *ii)* an effective volume-specific cathodic exchange current density, $(ai_0)_{\text{c,eff}}$, which should take into account the blockage of the active catalyst surface area due to the presence of adsorbates originated by the parasitic oxidation of ethanol and acetaldehyde at the cathode electrode, and to the presence of liquid water.

As shown in Fig. 1, the cell is divided into seven regions: anode channel (ac); anode gas diffusion layer (agdl); anode catalyst layer (acl); polymeric membrane (mem); cathode catalyst layer (ccl); cathode

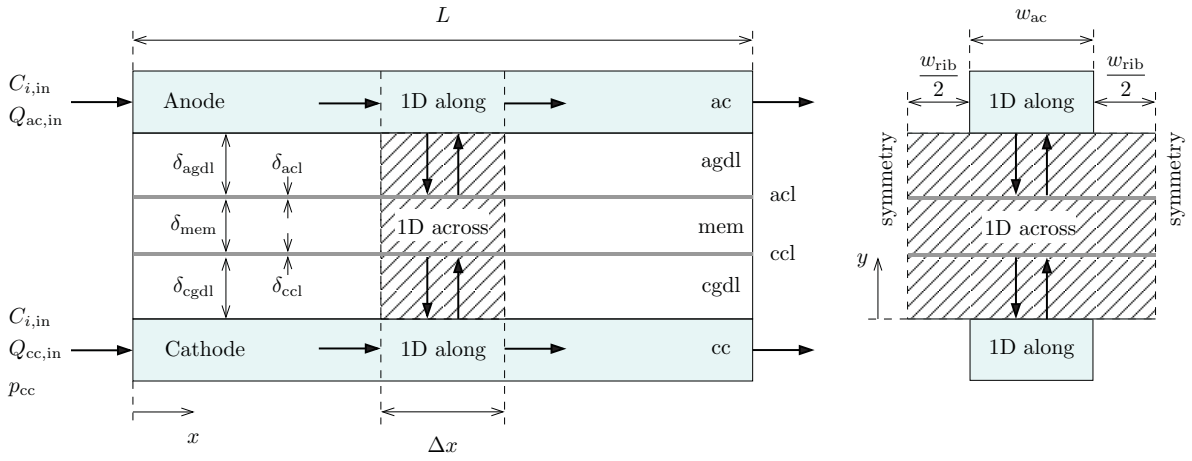

Figure 1: Schematic representation of the physical domains covered by the one-dimensional across- and along-the-channel models, showing the inlet conditions, the channel and rib dimensions (length, L, channel width, w_{ac}, and rib width, w_{rib}), and the thickness of the different layers of the MEA (δ_ℓ, ℓ = agdl, acl, mem, ccl, cgdl). Left: side view; right: cross-sectional view.

gas diffusion layer (cgdl); and cathode channel (cc). The figure also shows the domains covered by the 1D across-the-channel model, dominated by transverse diffusive fluxes and electro-osmotic drag through the MEA (agdl, acl, mem, ccl and cgdl), and the 1D along-the-channel model, dominated by longitudinal convective fluxes along the flow channels. It also shows the notation for the inlet conditions at the anode and cathode channels, and the thickness of the different layers of the MEA.

3. 1D across-the-channel model

The 1D across-the-channel model presented below is based on the DEFC anode model developed in [66], which is here extended to include also the cathode electrode.

3.1. Anode electrode

The anode electrode is modeled using the detailed kinetic model recently presented by the authors [66]. As shown schematically in Fig. 2, the reaction mechanism includes eleven elementary reaction, five of them reversible, which involve five adsorbates (CH_3CHOH_{ads}, CH_3CO_{ads}, CO_{ads}, $CH_{3\,\mathrm{ads}}$, and OH) and six free species, including two reactants (water (W) and ethanol (E)) and four products (acetaldehyde (A), acetic acid (AA), CO_2 and CH_4). The stoichiometries of the elementary reactions and the values of the kinetic constants are summarized in Table 1. The resulting mathematical problem, outlined in the Appendix for reference purposes, provides the coverage factors of the adsorbates, Θ_j, the rate of the elementary reactions, q_r, the net production (+) or consumption (−) rates of the free species, ω_k, the cell

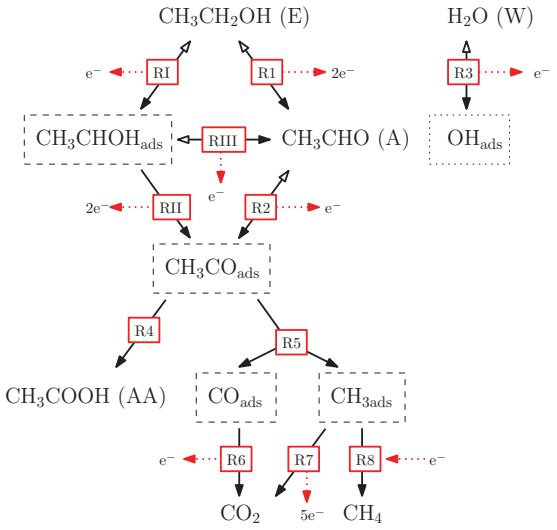

Figure 2: Reaction mechanism for the ethanol oxidation reaction on binary Pt-based catalysts considered in this work. The exact stoichiometries and the values of the kinetic constants are indicated in Table 1.

current density, i, the product selectivities

$$s_k = \frac{\omega_k}{\omega_{\mathrm{A}} + \omega_{\mathrm{AA}} + \omega_{\mathrm{CO_2}} + \omega_{\mathrm{CH_4}}} \qquad k = \mathrm{A}, \mathrm{AA}, \mathrm{CO_2}, \mathrm{CH_4} \tag{2}$$

and the average number of electrons transferred per ethanol molecule [66]

$$n^{\mathrm{eff}} = \frac{2s_{\mathrm{A}} + 4s_{\mathrm{AA}} + 6s_{\mathrm{CO_2}} - 2s_{\mathrm{CH_4}}}{1 - \frac{1}{2}\left(s_{\mathrm{CO_2}} + s_{\mathrm{CH_4}}\right)} \tag{3}$$

The inputs required by the model are the anode overpotential, the local concentrations of ethanol and acetaldehyde at the anode channel, the cell temperature, and the full set of kinetic constants shown in Table 1. This set was optimized using a multi-objective genetic algorithm so as to fit the anode polarization and product selectivity data reported by Li & Pickup [74] for all the current densities under study. This work introduces only one minor change, which is to ignore the production of methane via Reaction 8. This is achieved simply by setting $k_8 = 0$ in the reaction mechanism shown in Table 1, an approach that is well justified given the exceedingly small quantities of methane predicted by the full reaction mechanism [66].

3.2. Cathode electrode

Unlike the detailed kinetic description used in the anode electrode, the ORR is modeled as a single reversible reaction with Butler-Volmer kinetics. Species mass transport across the cathode gas diffusion layer is assumed to take place purely by gaseous diffusion. No attempt has been made to account for

Table 1: The 11-step reaction mechanism used in this work [66].

Reaction			n_α
I. $CH_3CH_2OH \rightleftharpoons CH_3CHOH_{ads} + H^+ + e^-$	k_{If} [s^{-1}] = 0.3306	$\alpha_I = 0.325$	1
	k_{Ib} [mol m^{-3} s^{-1}] = 1.8×10^{-3}		1
II. $CH_3CHOH_{ads} \rightarrow CH_3CO_{ads} + 2H^+ + 2e^-$	k_{II} [mol m^{-3} s^{-1}] = 1.34×10^2	$\alpha_{II} = 0.473$	2
III. $CH_3CHOH_{ads} \rightleftharpoons CH_3CHO + H^+ + e^-$	k_{IIIf} [mol m^{-3} s^{-1}] = 1.01×10^3	$\alpha_{III} = 0.362$	1
	k_{IIIb} [s^{-1}] = 22.67		1
1. $CH_3CH_2OH \rightleftharpoons CH_3CHO + 2H^+ + 2e^-$	k_{1f} [s^{-1}] = 3.49×10^{-5}	$\alpha_1 = 0.499$	2
	k_{1b} [s^{-1}] = 13.784		2
2. $CH_3CHO \rightleftharpoons CH_3CO_{ads} + H^+ + e^-$	k_{2f} [s^{-1}] = 6.4×10^{-2}	$\alpha_2 = 0.359$	1
	k_{2b} [mol m^{-3} s^{-1}] = 10^{-4}		1
3. $H_2O \rightleftharpoons OH_{ads} + H^+ + e^-$	k_{3f} [mol m^{-3} s^{-1}] = 0.9619	$\alpha_3 = 0.355$	1
	k_{3b} [mol m^{-3} s^{-1}] = 1.01×10^2		1
4. $CH_3CO_{ads} + OH_{ads} \longrightarrow CH_3COOH$	k_4 [mol m^{-3} s^{-1}] = 2.77×10^2		
5. $CH_3CO_{ads} \longrightarrow CO_{ads} + CH_{3\,ads}$	k_5 [mol m^{-3} s^{-1}] = 5.67		
6. $CO_{ads} + OH_{ads} \longrightarrow CO_2 + H^+ + e^-$	k_6 [mol m^{-3} s^{-1}] = 0.1391	$\alpha_6 = 0.319$	1
7. $CH_{3\,ads} + 2OH_{ads} \longrightarrow CO_2 + 5H^+ + 5e^-$	k_7 [mol m^{-3} s^{-1}] = 9.2	$\alpha_7 = 0.427$	5
8. $CH_{3\,ads} + H^+ + e^- \longrightarrow CH_4$	k_8 [mol m^{-3} s^{-1}] = 0	$\alpha_8 = 0.423$	1

multiphase flow effects, neither in the anode (CO_2 evolution) nor in the cathode (production and crossover of liquid water), as DEFC performance is known to be limited mainly by the sluggish kinetics of the EOR.

3.2.1. Cathode catalyst layer (ccl)

The ORR is be modeled as a single reversible global reaction

$$O_2 + 4H^+ + 4e^- \rightleftharpoons 2H_2O \tag{4}$$

with the corresponding oxygen consumption rate given by Butler-Volmer kinetics

$$q_{O_2} = (1 - s_c)(1 - \Theta_c)\frac{(ai_0)_c}{4F}\frac{C_{O_2,ccl}}{C_{O_2,ref}}\left[\exp\left(\frac{2\alpha F\eta_c}{RT}\right) - \exp\left(-\frac{2(1-\alpha)F\eta_c}{RT}\right)\right] \tag{5}$$

where $C_{O_2,ref}$ is the reference molar concentration of oxygen in air at standard conditions, a_c is the effective catalyst surface area per unit volume, and $i_{0,c}$ is the exchange current density of the cathodic reaction. The overall cathode coverage factor Θ_c accounts for the blockage of the active catalyst sites by the adsorbed species generated in the parasitic electro-oxidation of ethanol and acetaldehyde (e.g., CO poisoning), and by the OH-groups adsorbed at high cathode overpotentials. The presence of liquid water

at the cathode, which also contributes to the blockage of the catalyst surface area, is accounted for by the factor $(1 - s_c)$, where s_c represents the overall saturation of liquid water at the cathode catalyst layer.

The net reaction rate q_{O_2} given above stands for the number of moles of oxygen consumed by the ORR per unit volume and unit time. According to the stoichiometry of the global reaction (4), the overall current density generated at the cathode is thus given by

$$i_c = 4F\delta_{ccl}q_{O_2} \tag{6}$$

which must be equal to the sum of the current produced by the anodic reaction, i, plus the parasitic current density, i_p, generated by the electro-oxidation of the free species that cross the membrane from anode to cathode

$$i_c = i + i_p \tag{7}$$

It is important to note that the factor δ_{ccl} appearing in (6) represents the thickness of the cathode catalyst layer, where the reaction rate q_{O_2} is considered to be spatially uniform according to assumption *v*).

The transfer coefficient α appearing in (5) is taken here to be equal to 0.5. In this case, the Butler-Volmer equation (5) can be rewritten as

$$q_{O_2} = \frac{(ai_0)_{c,eff}}{2F}\frac{C_{O_2,ccl}}{C_{O_2,ref}}\sinh\left(\frac{F\eta_c}{RT}\right) \tag{8}$$

which, together with Eq. (6), leads to the following closed-form analytical expression for the cathode overpotential

$$\eta_c = \frac{RT}{F}\sinh^{-1}\left(\frac{1}{2\delta_{ccl}}\frac{i_c}{(ai_0)_{c,eff}}\frac{C_{O_2,ref}}{C_{O_2,ccl}}\right) \tag{9}$$

in terms of the cathode current density, i_c, and the concentration of oxygen at the cathode catalyst layer, $C_{O_2,ccl}$.

To abbreviate the notation, the last two equations have been written in terms of the lumped parameter

$$(ai_0)_{c,eff} = (1 - s_c)(1 - \Theta_c)(ai_0)_c \tag{10}$$

which can be viewed as an effective volume-specific cathodic exchange current density. This parameter takes into account the detrimental effect caused by the blockage of the active catalyst sites due to the presence of liquid water and of the strongly adsorbed species produced by the parasitic electro-oxidation reactions, and is one of the two adjustable parameters that will be fitted using experimental results.

3.2.2. Cathode gas diffusion layer (cgdl)

The molar flux of species k, transported by convection and diffusion from the bulk fluid in the cathode channel (cc) to the cathode channel/gas diffusion layer interface, and from there only by diffusion across the cathode gas diffusion layer (cgdl) to the cathode catalyst layer (ccl), is computed using an overall mass transport coefficient $\mathfrak{h}_c$ such that

$$N_k = \mathfrak{h}_c \left(C_{k,\mathrm{cc}} - C_{k,\mathrm{ccl}}\right) \qquad k = \mathrm{O_2},\ \mathrm{W},\ \mathrm{AA} \tag{11}$$

where $C_{k,\mathrm{cc}}$ is the bulk concentration of species k in the cathode channel, and $C_{k,\mathrm{ccl}}$ is the effective concentration of species k at the cathode catalyst layer. Like in Chapter 3, the sign of N_k indicates whether the molar flux of species k is directed in the positive or negative y-direction. However, due to the different relative positions of the channel and the catalyst layer, in the cathode the net flux of species k is directed towards the catalyst layer for $N_k > 0$ and towards the channel for $N_k < 0$.

The effect of convective drag in the cathode gas diffusion layer is anticipated to be small, just like in the anode electrode, so it will be neglected. The global transport coefficient of oxygen can then be written as

$$\mathfrak{h}_c = \left(\frac{1}{h} + \frac{\delta_{\mathrm{cgdl}}}{D^{\mathrm{eff}}_{\mathrm{O_2,cgdl}}}\right)^{-1} \tag{12}$$

which combines the effect of convective and diffusive transport in the cathode flow channel, characterized by the overall convective coefficient h, and Fickian diffusion in the cathode gas diffusion layer through the diffusive transport coefficient $D^{\mathrm{eff}}_{\mathrm{O_2,cgdl}}/\delta_{\mathrm{cgdl}}$. Like in the anode model presented in Chapter 3, the Bruggeman correction is used to calculate the effective diffusivity, $D_{\mathrm{O_2,cgdl}} = \epsilon^{3/2} D_{\mathrm{O_2,air}}$, in terms of the porosity ϵ of the cathode gas diffusion layer and of the bulk diffusivity $D_{\mathrm{O_2,air}}$ of oxygen in air.

Species conservation dictates that, in the absence of oxygen crossover, whose effect is neglected here for simplicity [66], the molar flux of oxygen that reaches the cathode catalyst layer from the cathode flow channel must be equal to the rate of oxygen consumption by the electrochemical reactions

$$N_{\mathrm{O_2}} = \frac{i_c}{4F} \tag{13}$$

Combining Eqs. (11) and (13) leads to the following expression for the concentration of oxygen at the cathode catalyst layer

$$C_{\mathrm{O_2,ccl}} = C_{\mathrm{O_2,cc}} - \frac{1}{\mathfrak{h}_c}\frac{i_c}{4F} \tag{14}$$

which can be used in (9) to determine the cathode overpotential η_c for given values of $C_{\mathrm{O_2,cc}}$ and i_c.

The water produced by the ORR plus the flux water that crosses the membrane by electro-osmotic drag must both be evacuated through the cathode gas diffusion layer to the cathode channel. Assuming that all water is transported in the form of water vapor, the total flux of water (W) that emerges from the cathode catalyst layer towards the cathode gas diffusion layer can be written as

$$N_{\mathrm{W}} = N_{\mathrm{W,cross}} - \left(\frac{i}{2F} + n_d^{\mathrm{W}} \frac{i}{F} \right) \tag{15}$$

where the first term represents the molar flux of water generated by the oxidation of the crossover species, to be evaluated next, the second term is the water produced by the ORR due to the output current density, and the last term is the electroosmotic drag of water that crosses the membrane from anode to cathode.

3.3. Species crossover

As already discussed, the permeation of ethanol and other species through the polymeric membrane constitutes a severe problem for DEFC performance, which is accentuated at low current densities [75]. The reason is that the reactive species that cross the membrane are prone to react electrochemically with oxygen at the cathode catalyst layer, which results in a parasitic current that increases the cathode overpotential [49]. Oxygen crossover may also result in the parasitic oxidation of ethanol at the anode [76], but the quantitative effect is anticipated to be small and can be neglected in first approximation [66].

For the sake of simplicity, the present model will only consider the effects of ethanol and acetaldehyde crossover, as in low-temperature DEFCs they represent the two major reacting species generating electrons during the electro-oxidation process. Additionally, because the cathode potential is always higher than the anode potential, the overpotential η_{c} of the cathodic parasitic reactions is higher than that of the anodic oxidation reactions. Thus, the parasitic oxidation of ethanol and acetaldehyde will be assumed to proceed to completion, yielding acetic acid as final product through the overall reactions

$$\mathrm{CH_3CH_2OH + O_2 \rightarrow CH_3COOH + H_2O} \tag{16}$$

$$\mathrm{CH_3CHO + \frac{1}{2}O_2 \rightarrow CH_3COOH} \tag{17}$$

involving the transfer of 4 and 2 electrons, respectively. Introducing further complexity in the crossover model would not be reasonable at this point given the difficulty of measuring the product distributions accurately from a DEFC, as would be required for the validation of a more complex model [32].

The parasitic current density induced at the cathode catalyst layer by crossover can be obtained as the sum of the ethanol and acetaldehyde parasitic current densities

$$i_p = i_{\mathrm{E},p} + i_{\mathrm{A},p} \tag{18}$$

According to the global stoichiometries of reactions (16) and (17), the ethanol and acetaldehyde parasitic current densities can be expressed as

$$i_{\mathrm{E},p} = -4FN_{\mathrm{E,cross}} \quad \text{and} \quad i_{\mathrm{A},p} = -2FN_{\mathrm{A,cross}} \tag{19}$$

in terms of the corresponding crossover fluxes, given by (A.26) in the Appendix. The assumption that both ethanol and acetaldehyde are completely oxidized to acetic acid is in agreement with the values $n^{\mathrm{eff}} \simeq 4$ reported in [66] under the same conditions considered in this work. According to Figure 1, the crossover fluxes $N_{\mathrm{E,cross}}$ and $N_{\mathrm{A,cross}}$ must be negative, because ethanol and acetaldehyde cross the membrane from anode to cathode in the negative y-direction, which motivates the minus signs in (19).

According to reaction (16), the electro-oxidation of ethanol to acetic acid produces one mole of acetic acid and one mole of water per mole of ethanol. In consequence, the molar production rates due to the parasitic oxidation of ethanol (E) in the cathode catalyst are given by

$$\omega^{(\mathrm{E})}_{\mathrm{W,c}} = \omega^{(\mathrm{E})}_{\mathrm{AA,c}} = -N_{\mathrm{E,cross}} = \frac{i_{\mathrm{E},p}}{4F} \tag{20}$$

By contrast, the electro-oxidation of acetaldehyde to acetic acid through reaction (17) does not produce water. In this case, the molar production rate of acetic acid due to the parasitic oxidation of acetaldehyde (A) at the cathode catalyst layer is given by

$$\omega^{(\mathrm{A})}_{\mathrm{AA,c}} = -N_{\mathrm{A,cross}} = \frac{i_{\mathrm{A},p}}{2F} \tag{21}$$

The molar flux of water induced by the electrooxidation of the crossover species at the cathode catalyst layer is thus limited to the contribution of the parasitic oxidation of ethanol

$$N_{\mathrm{W,cross}} = -\omega^{(\mathrm{E})}_{\mathrm{W,c}} = -\frac{i_{\mathrm{E},p}}{4F} \tag{22}$$

Substituting the last expression in Eq. (15), the net molar flux of water leaving the cathode catalyst layer can be written as

$$N_{\mathrm{W}} = -\left(\frac{i_{\mathrm{E},p}}{4F} + \frac{i}{2F} + n_d^{\mathrm{W}}\frac{i}{F}\right) \tag{23}$$

in terms of the parasitic current density induced by ethanol crossover, $i_{\mathrm{E},p}$, and the net current density, i, generated by the cell. Similarly, the net molar production rate of acetic acid at the cathode catalyst layer is obtained adding the contributions due to ethanol and acetaldehyde crossover

$$\omega_{\mathrm{AA,c}} = \omega^{(\mathrm{E})}_{\mathrm{AA,c}} + \omega^{(\mathrm{A})}_{\mathrm{AA,c}} \tag{24}$$

3.4. Solution procedure

This section summarizes the procedure used to solve the mathematical problem stated in the previous sections. The cornerstone that closes the problem is the equation for the cell voltage, V, which is given by

$$V = E_{\text{cell}} - \eta_{\text{a}} - \eta_{\text{c}} - \eta_{\text{ohm}} \tag{25}$$

in terms of the cell reversible potential, E_{cell}, the anode overpotential, η_{a}, the cathode overpotential, η_{c}, and the ohmic overpotentital

$$\eta_{\text{ohm}} = i\,(R_{\text{mem}} + R_{\text{cont}}) \tag{26}$$

written here in terms of the protonic resistance of the membrane, $R_{\text{mem}} = \delta_{\text{mem}}/\sigma_{\text{mem}}$, and the effective electronic/contact resistance, R_{cont}, which accounts for the ohmic losses due to all cell elements other than the polymeric membrane along with their interfaces. The ionic conductivity of the membrane is evaluated as [77]

$$\sigma_{\text{mem}} = \sigma^0_{\text{mem}} \exp\left[1268\left(\frac{1}{298} - \frac{1}{T}\right)\right] \tag{27}$$

in terms of the temperature of operation, T, and the reference conductivity at 298 K, $\sigma^0_{\text{mem}} = 7.3$ S m^{-1}.

At a particular channel section, the solution procedure starts with the concentrations of ethanol and acetaldehyde in the anode channel, $C_{\text{E,ac}}$ and $C_{\text{A,ac}}$, and the concentration of oxygen in the cathode channel, $C_{\text{O}_2\text{,cc}}$, which are considered to be known. As a result, for the cell voltage under consideration, V, Eq. (25) can be rewritten as follows

$$f\,(\eta_{\text{a}}; C_{\text{E,ac}}, C_{\text{A,ac}}, C_{\text{O}_2\text{,cc}}, V) \equiv E_{\text{cell}} - V - \eta_{\text{a}} - \eta_{\text{c}}(C_{\text{O}_2\text{,cc}}, i_{\text{c}}\,(C_{\text{E,ac}}, C_{\text{A,ac}}, \eta_{\text{a}})) - i\,(C_{\text{E,ac}}, C_{\text{A,ac}}, \eta_{\text{a}})\,(R_{\text{mem}} + R_{\text{cont}}) = 0 \tag{28}$$

where the variation of the cathode overpotential with $C_{\text{O}_2\text{,cc}}$ and i_{c} is given analytically by Eq. (9), while the explicit dependencies of the current densities i and i_{c} as a function of $C_{\text{E,ac}}$, $C_{\text{A,ac}}$ and η_{a} result from the solution of the 1D anode model (see Appendix for details), which provides the output current density i and enables the computation of i_{c} through Eqs (7), (18) and (19).

For fixed values of $C_{\text{E,ac}}$, $C_{\text{A,ac}}$, $C_{\text{O}_2\text{,cc}}$ and V, the nonlinear algebraic equation (28) can be solved for the anode overpotential η_{a} using, for instance, a Newton-Raphson method. This method requires the evaluation of the derivative of f with respect to η_{a}, which can be written by applying the chain rule as

$$\frac{\mathrm{d}f}{\mathrm{d}\eta_{\text{a}}} = -1 - \frac{\mathrm{d}\eta_{\text{c}}}{\mathrm{d}i_{\text{c}}}\frac{\mathrm{d}i_{\text{c}}}{\mathrm{d}\eta_{\text{a}}} - \frac{\mathrm{d}i}{\mathrm{d}\eta_{\text{a}}}(R_{\text{mem}} + R_{\text{cont}}) \tag{29}$$

From Eq. (9), the derivative of η_c with respect to i_c can be written analytically as

$$\frac{\mathrm{d}\eta_c}{\mathrm{d}i_c} = \frac{(RT/F)}{2\delta_{ccl}} \frac{C_{O_2,ref}}{(ai_0)_{c,eff}} \left\{ 1 + \left[\frac{1}{2\delta_{ccl}} \frac{i_c}{(ai_0)_{c,eff}} \frac{C_{O_2,ref}}{C_{O_2,ccl}} \right]^2 \right\}^{-1/2} \left[\frac{C_{O_2,ccl} + i_c/(4F\mathfrak{h}_c)}{C^2_{O_2,ccl}} \right] \tag{30}$$

whereas the derivatives of the current densities i and i_c with respect to η_a have to be evaluated numerically by solving the anode problem formulated in the Appendix for two neighboring values of η_a and applying the definition of partial derivative, namely

$$\frac{\mathrm{d}i}{\mathrm{d}\eta_a} \approx \frac{i\left(C_{E,ac}, C_{A,ac}, \eta_a + \Delta\eta_a\right) - i\left(C_{E,ac}, C_{A,ac}, \eta_a\right)}{\Delta\eta_a} \quad \text{with} \quad \Delta\eta_a \ll \eta_a \tag{31}$$

4. 1D-along the channel model

The electrochemical consumption and production of free species, combined with the redistribution effect of water and species crossover, makes the bulk fluid velocities and species concentrations to vary significatively along the flow channels, particularly for low anode and cathode stoichiometries. Such spatial variations can be determined, in first approximation, using a simplified one-dimensional advection model. The model is based on the discretization of the flow channels in a large number of elements, $N \gg 1$, such that the length of a single element, $\Delta x = L/N$, is much smaller than the full channel length, L. Applying the continuity and species mass conservation equations to the n-th channel element, $x \in (x_n, x_{n+1})$, $x_n = (n-1)\Delta x$, shown in Fig. 3, provides the recursive laws that govern the variation of the flow velocities and species concentrations along the flow channels, to be discussed below separately for the anode and cathode compartments.

These recursive laws involve the local transverse molar fluxes and water/gas velocities established in the anode and cathode gas diffusion layers, which are determined as part of the solution of the 1D across-the-channel model presented previously. Thus, given the local concentrations of ethanol, acetaldehyde and oxygen at their corresponding channel elements, $C^n_{E,ac}$, $C^n_{AA,ac}$ and $C^n_{O_2,cc}$, and the cell voltage, V, the procedure outlined in Section 3 yields the local overpotentials of the electrodes, which in turn determines the molar consumption/production rates of the differen species. Appropriate mass balances applied to the anode catalyst layers similar to those presented in the Appendix for ethanol and acetaldehyde, (A.27) and (A.28), provide the transverse molar fluxes of all the anodic active species, N^n_k, k = E, A, AA, CO_2, while the transverse molar fluxes of O_2 and W are given by Eqs. (13) and (23).

4.1. Anode channels

For the typical operating conditions of a DEFC, the Peclet number of the flow in the channels is of order 10^4 to 10^5 in the anode and 10^2 in the cathode. As a result, longitudinal diffusion can be safely

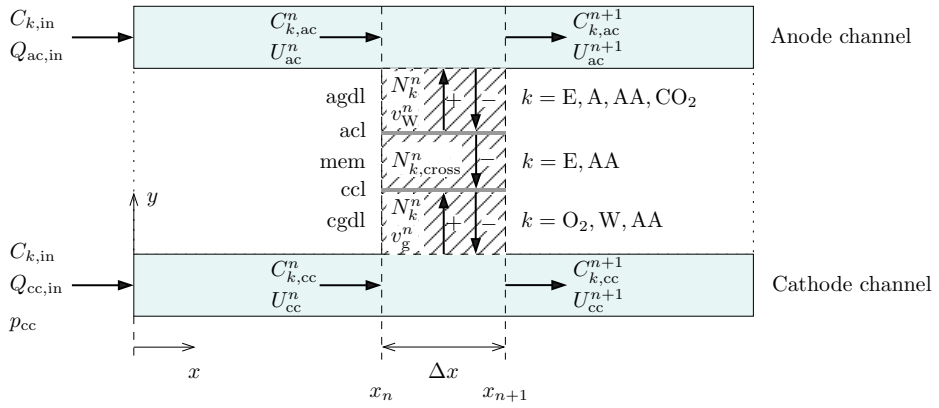

Figure 3: Schematic representation of the continuity equation and mass conservation equation of species k applied to the n-th channel element. The water velocity v^n_{W} must be used at the anode and the gas velocity v^n_{g} at the cathode.

neglected in both cases. Under these conditions, and considering steady state operation, the discretized continuity and species conservation equations for the channel element take the form

$$U^n_{\mathrm{ac}} h_{\mathrm{ch}} + v^n_{\mathrm{W}} \Delta x = \qquad U^{n+1}_{\mathrm{ac}} h_{\mathrm{ch}} \tag{32}$$

$$C^n_{k,\mathrm{ac}} U^n_{\mathrm{ac}} h_{\mathrm{ch}} + N^n_k \Delta x = C^{n+1}_{k,\mathrm{ac}} U^{n+1}_{\mathrm{ac}} h_{\mathrm{ch}} \tag{33}$$

where $U_{\mathrm{ac}} = Q_{\mathrm{ac}}/(w_{\mathrm{ch}} h_{\mathrm{ch}})$ and $C_{k,\mathrm{ac}}$ are the average water velocity and bulk molar concentration of species k in the anode channel, h_{ch} is the channel height, and v_{W} and N_k are the average transverse water velocity and molar flux of species k at the anode channel/gas diffusion layer interface. As previously discussed, the last two values are provided by the solution of the 1D across-the-channel model presented in Section 3. It should be noted that in the above equations the convective terms involve magnitudes that are averaged over the inlet and outlet of the channel element, $x = x_n$ or x_{n+1}, while the transverse transport terms involve magnitudes that are averaged over the n-th channel element/gas diffusion layer interface, as is sketched in Fig. 3.

Under the assumption of convectively dominated flow in the channels leading to Eqs. (32) and (33), the discrete channel elements can be solved successively from channel inlet to channel outlet. First, from Eq. (32) the average fluid velocity at $x = x_{n+1}$ can be expressed as

$$U^{n+1}_{\mathrm{ac}} = U^n_{\mathrm{ac}} + \frac{\Delta x}{h_{\mathrm{ch}}} v^n_{\mathrm{W}} \tag{34}$$

in terms of the average fluid velocity at the previous channel section, U^n_{ac}, and the average transverse water velocity at the n-th channel element, v^n_{W}. Substituting this expression into Eq. (33) provides the

concentration of species k at $x = x_{n+1}$

$$C_{k,\mathrm{ac}}^{n+1} = \left(C_{k,\mathrm{ac}}^{n} + \frac{\Delta x}{h_{\mathrm{ch}}}\frac{N_k^n}{U_{\mathrm{ac}}^n}\right)\left(1 + \frac{\Delta x}{h_{\mathrm{ch}}}\frac{v_{\mathrm{W}}^n}{U_{\mathrm{ac}}^n}\right)^{-1} \tag{35}$$

in terms of the concentration at $x = x_n$, $C_{k,\mathrm{ac}}^n$, and the average transverse molar flux of species k at the n-th channel element, N_k^n.

4.2. Cathode channels

The cathode flow channels can be treated similarly, except that in this case the working fluid is a mixture of ideal gases. Assuming that oxygen, water vapor and acetic acid are the only active species (i.e., electrochemically consumed or produced) that emerge from the cathode catalyst layer to the gas diffusion layer, the recursive laws that provide the flow velocity and species concentrations at $x = x_{n+1}$ from those at $x = x_n$ can be written as

$$U_{\mathrm{cc}}^{n+1} = U_{\mathrm{cc}}^{n} - \frac{\Delta x}{h_{\mathrm{ch}}} v_{\mathrm{g}}^n \tag{36}$$

and

$$C_{k,\mathrm{cc}}^{n+1} = \left(C_{k,\mathrm{cc}}^{n} - \frac{\Delta x}{h_{\mathrm{ch}}}\frac{N_k^n}{U_{\mathrm{cc}}^n}\right)\left(1 - \frac{\Delta x}{h_{\mathrm{ch}}}\frac{v_{\mathrm{g}}^n}{U_{\mathrm{cc}}^n}\right)^{-1} \tag{37}$$

Note that the role played in the anode by the water flux velocity v_{W} is assumed in the cathode by the average gas velocity

$$\begin{aligned} v_{\mathrm{g}} &= \frac{RT}{p_{\mathrm{c}}}\left(N_{\mathrm{O_2}} + N_{\mathrm{W}} + N_{\mathrm{AA}}\right) \\ &= \frac{RT}{p_{\mathrm{c}}}\left[\frac{i_{\mathrm{c}}}{4F} - \left(\frac{i_{\mathrm{E},p}}{4F} + \frac{i}{2F} + n_d^{\mathrm{W}}\frac{i}{F}\right) - \left(\frac{i_{\mathrm{E},p}}{4F} + \frac{i_{\mathrm{A},p}}{2F}\right)\right] \\ &= -\frac{RT}{p_{\mathrm{c}}}\left(\frac{i + i_{\mathrm{E},p} + i_{\mathrm{A},p}}{4F} + n_d^{\mathrm{W}}\frac{i}{F}\right) \end{aligned} \tag{38}$$

expressed here in terms of the output and parasitic current densities i, $i_{\mathrm{E},p}$ and $i_{\mathrm{A},p}$ with use made of Eqs. (13), (18), (23) and (24).

It is important to note that according to (38) the transverse gas velocity v_{g} is always negative, meaning that it will contribute to accelerate the gas flow along the cathode channel. This is true even under open circuit conditions ($i = 0$), when there is still a net source of gas due to the production of water and acetic acid by the parasitic electrooxidation of ethanol and acetaldehyde. For non-zero current densities the water crossover term soon becomes dominant due to the high water permeation rates typical of fully humidified Nafion membranes ($n_{\mathrm{w}} \sim 2.5 - 3$). This leads to increasingly large gas production rates along the cathode channels, which may result in the emergence of a certain amount of liquid water under appropriate conditions.

5. Model fitting procedure

A simulation campaign was performed to optimize the predictive capabilities of the model using selected experimental data reported in the literature. To be consistent with the optimization of the anode reaction mechanism carried out previously [66], which used the experimental anode polarization data by Li & Pickup [74], the cell polarization curve obtained in those same experiments was used here as target data. All the simulations were carried out with a fixed set of physical constants, mass transport properties and design parameters, indicated in Tables 2 and 3.

A genetic optimization algorithm was used to determine the values of the volume-specific effective cathode exchange current density, $(ai_0)_{\mathrm{c,eff}}$, and the overall cell electronic/contact resistance, R_{cont}. The objective function used was the root-mean-square error of the computed current density corresponding to a set of cell voltages reported experimentally

$$\mathrm{err} = \sqrt{\sum_i \left(\frac{x_{i,\mathrm{LP}} - x_i}{x_{i,\mathrm{LP}}} \right)^2} \tag{39}$$

where $x_{i,\mathrm{LP}}$ denotes the experimental current density measurements reported by Li & Pickup [74]. To avoid spurious results, only the data corresponding to cell voltages equal or smaller than 0.4 V were considered in the model fitting process. The values of $(ai_0)_{\mathrm{c,eff}}$ and R_{cont} thus obtained are also included in Table 2.

Figure 4 shows the polarization curve, along with the anode overpotential and cathode potential vs.

Table 2: Physical constants, convective mass transport coefficient and geometrical parameters used in the 1D across-the-channel model. The fitted parameters $(ai_0)_{\mathrm{c,eff}}$ and R_{cont} provided by the optimization algorithm are also shown for reference purposes.

Property	Value	Reference
α	0.50	[78]
$C_{\mathrm{O_2,ref}}$	8.73 mol/m^3	Assumed
$D_{\mathrm{O_2,air}}$	$2.5 \times 10^{-5} \left(\frac{T}{298}\right)^{3/2} \left(\frac{p_{amb}}{p}\right)$ m^{2}s^{-1}	[79]
h	10^{-2} m s^{-1}	Assumed
ϵ	0.78	[54]
δ_{agdl}	280 μm	[54]
δ_{acl}	20 μm	[54]
δ_{mem}	178 μm	[54]
$(ai_0)_{\mathrm{c,eff}}$	6.816 A/m^3	Fitted
R_{cont}	1.5056×10^{-4} Ωm^2	Fitted

Table 3: Geometrical and operational parameters used in the 1D along-the-channel model.

Property	Value
Rib width, w_{rib}	1 mm
Channel width, w_{ch}	1 mm
Channel height, h_{ch}	0.7 mm
Cell surface area, S	5 cm^2
Effective channel length, L	$S/(w_{\mathrm{rib}} + w_{\mathrm{ch}}) = 0.25$ m
Anode volume flow rate, $Q_{\mathrm{ac,in}}$	5 ml min^{-1}
Cathode volume flow rate, $Q_{\mathrm{cc,in}}$	60 ml min^{-1}
Ethanol feed concentration, $C_{\mathrm{E,in}}$	1 M
Oxygen feed concentration, $C_{\mathrm{O_2,in}}$	10.22 mol/m^3
Cathode pressure, p_{c}	1.5 bar
Cell Temperature, T	80°C

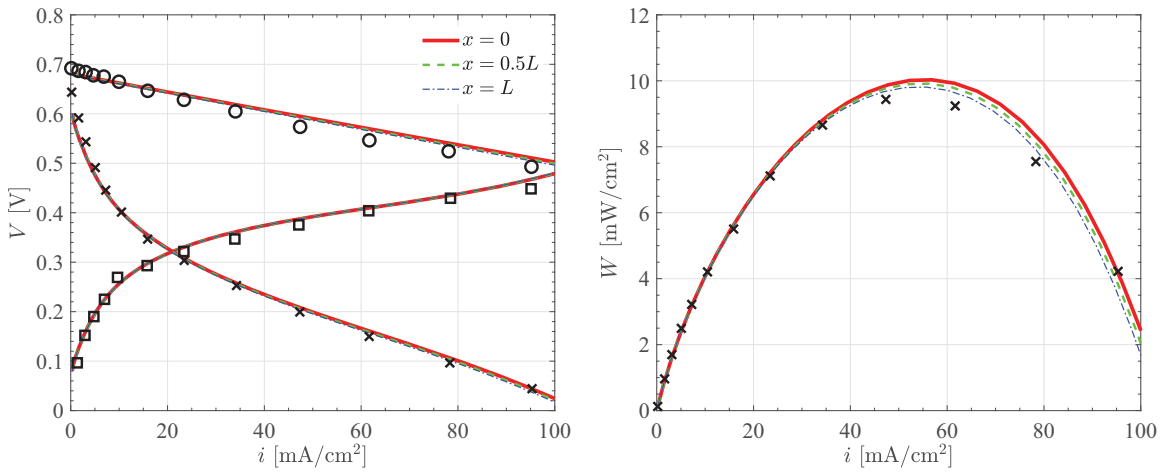

Figure 4: Left: cell voltage (×), cathode potential (O) and anode overpotential (□) reported by [74] and computed with the present model (solid, dashed and dash-dotted lines, respectively) at different sections along the flow channels as indicated in the legends. Right: computed (solid lines) and experimental (×) power density curves corresponding to the polarization data shown on the left.

current density curves, computed at different sections along the flow channels using the optimized 1D + 1D model and measured experimentally. The corresponding power density curves are also shown for comparison. The model results show that with the operational conditions considered in the experimental setup of Li & Pickup [74] the variation of performance along the flow channels is almost negligible. In general, the model correctly predicts the cell current density in the whole range of cell voltages, and there

is also satisfactory agreement both with the anode and cathode overpotentials. The anode overpotential was already optimized in Chapter 3, so the good agreement was to be expected. The optimization of the effective cathode exchange current density, $(ai_0)_{c,eff}$, and overall electronic/contact resistance, R_{cont}, carried out in this work result also in an excellent agreement in the cathode potential and cell polarization curves.

Before proceeding further, it is instructive to comment on the values obtained for the fitted parameters and extract some preliminary conclusions from them. First, the electronic/contact resistance reported in Table 2 is about ten times larger than the ionic resistance of the membrane, $R_{cont}/R_{mem} = 10.75$, meaning that in the experimental setup of Li & Pickup [74] the contact resistances were not sufficiently minimized. Second, the fitted effective cathode exchange current density is much smaller than expected in the absence of poisoning and/or cathode flooding effects. Considering, for instance, typical values of $a_c = 6 \times 10^4$ m^{-1} and $i_{0,c} = 0.04222$ A m^{-2} [80], the volume specific cathode exchange current density would be of order $(ai_0)_c \sim 2.5 \times 10^3$ A m^{-3}, meaning that

$$\frac{(ai_0)_{c,eff}}{(ai_0)_c} = (1 - s_c)(1 - \Theta_c) \sim 2.7 \times 10^{-3} \tag{40}$$

Assuming that the presence of liquid water reduces only the catalyst active area by a factor of order unity, $(1 - s_c) \sim 1$, the above estimation shows that $(1 - \Theta_c) \lesssim 10^{-2}$, indicating that the overall cathode coverage factor Θ_c would be 0.99 or larger. Briefly speaking, one could expect that in an operating DEFC such as the one employed by Li & Pickup [74] more than 99% of the active catalyst sites of the cathode electrode would be unavailable for the ORR. Such a reduced active area could be attributed to a high occupation of the cathode catalyst sites by intermediate adsorbates of the parasitic oxidation of ethanol and acetaldehyde. The negative impact of crossover is therefore twofold, as it not only creates the parasitic current density that increases the cathode overpotential, but also reduces the cathode activity towards the ORR raising the cathode overpotential even further.

To emphasize the validity of the model fitting procedure, a second validation campaign was carried out using in this case the experimental results of Meyer et al. [54]. Figure 5 shows polarization curves and electrode potentials obtained experimentally (symbols) [54] and simulated with the current model (line plots) for different ethanol feed concentrations and a cell temperature of 70°C. The operating and design parameters of the cell were conveniently adapted to the experimental conditions: $Q_{ac,in} = 5.7$ ml/min, $Q_{cc,in} = 250$ ml/min, $p_c = 1$ bar, $S = 23.79$ cm^2, $\delta_{acl} = 12$ μm, $(ai_0)_{c,eff} = 1.363$ A/m^3, $R_{cont} = 3.0112 \times 10^{-4}$ Ωm^2. Compared to the set of parameters indicated in Tables 2 and 3, these values include a lower effective cathode exchange current density, thinner catalyst layers, and a higher contact resistance, resulting in a poorer cell performance. This is most likely due to the lower catalyst loading ca. 1.14

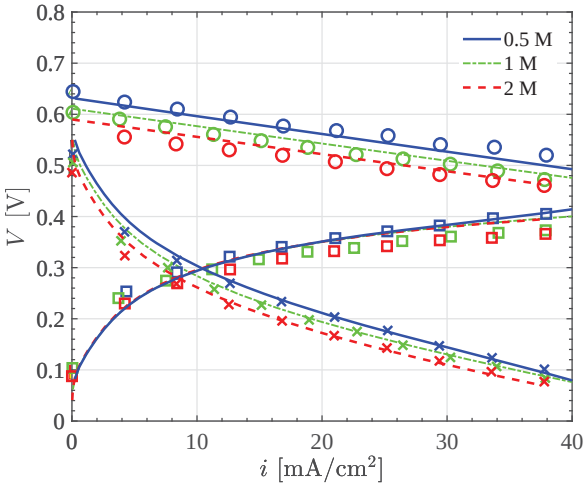

Figure 5: Left: cell voltage (×), cathode potential (O) and anode overpotential (□) reported by [54] (symbols) and computed with the present model (lines) for different ethanol feed concentrations.

mg/cm^2 used in the experimental setup of Meyer et al. [54] compared to the ca. 4.5 mg/cm^2 employed by Li & Pickup [74], and to the slightly lower cell temperature, 70°C vs. 80°C. The results confirm the capability of the model to reproduce experimental data for different cell set-ups and operating conditions.

6. Results and discussion

Once the model has been optimized to fit the experimental results, a parametric study will be carried out to asses the effect of two of the main operational parameters that influence cell performance: the anode flow rate and ethanol feed concentration. If either of them decreases sufficiently, cell performance starts to be affected by ethanol depletion, an effect that becomes more serious at low cell voltages. As ethanol becomes scarce downstream the channels, the cell starts to use the acetaldehyde produced upstream, which results in an interesting evolution of species concentrations as will be shown below.

6.1. Downstream evolution along the flow channel

To accentuate the effect of ethanol depletion, a cell with larger active surface area and lower anode feed flow rate than the cell used for model fitting will be considered. Table 4 summarizes the modified design and operational parameters considered in the following study, the other parameters being taken from Tables 2 and 3. Compared to the initial values used in the model fitting procedure there is a fivefold increase in the cell surface area. This in turn translates into a fivefold growth in the effective channel length, under the assumption of a single serpentine flow field with equal channel cross-section. In addition, the anode feed flow rate is reduced by a factor $5/0.3 \simeq 16.7$. The significantly smaller anode

stoichiometry (reduced by a factor of ca. 83 compared to that of Li & Pickup [74]) results in a more pronounced reduction of ethanol concentration along the flow channels, which induces an interesting evolution of the concentrations of other species, such as acetaldehyde or acetic acid, but also of the local cell and parasitic current densities.

Figure 6 shows the polarization curve, along with the anode overpotential and cathode potential vs. current density curves, computed at different sections along the flow channels. The differences between channel inlet and outlet become significant at mid-to-low voltages (i.e., mid-to-high currents), when ethanol depletion starts to affect the cell performance. For instance, at 0.1 V the current density drops about 17 mA/cm^2 from channel inlet to channel outlet. The maximum power density is obtained at the channel inlet corresponding to a cell voltage of 0.19 V. Note that the cathode potential is hardly affected by ethanol depletion in these conditions. It should be noted that the polarization curves calculated in different sections of the channel are not independent of each other, because an increased consumption of ethanol upstream translates into less ethanol available downstream. As a result, while at the channel inlet the local current density increases monotonically as the cell voltage is decreased, in later sections the polarization and power curves behave differently, and below a certain threshold voltage the local current density starts to decrease as well.

Figure 7 shows the evolution of the cell current density along the flow channels. It can be seen that at low cell potentials the reduction in the cell current density is sharper towards the end of the channel. The blue marks indicate the channel section that generates the average current density. At cell voltages lower than ca. 0.1 V its position is sightly displaced downstream the mid channel section as a result of the nonlinear reduction of the current density along the channel length. Figure 7 shows also the ratio between the current density and the average current density for different cell voltages. The relative variation is between ca. 10% for high cell voltages (including the voltage at maximum power density) to over 20% at lower cell voltages. For instance, at 0.05 V the current density at the channel inlet is 19% larger than the average current density, while at the channel exit it is 26% lower than the average value.

Table 4: Design and operational parameters used for model fitting and for the parametric study.

Property	Model fitting [74]	Parametric study
Cell surface area, S	5 cm^2	25 cm^2
Effective channel length, L	0.25 m	$S/(w_{\mathrm{rib}} + w_{\mathrm{ch}})$ =1.25 m
Anode volume flow rate	5 ml min^{-1}	0.3 ml min^{-1}

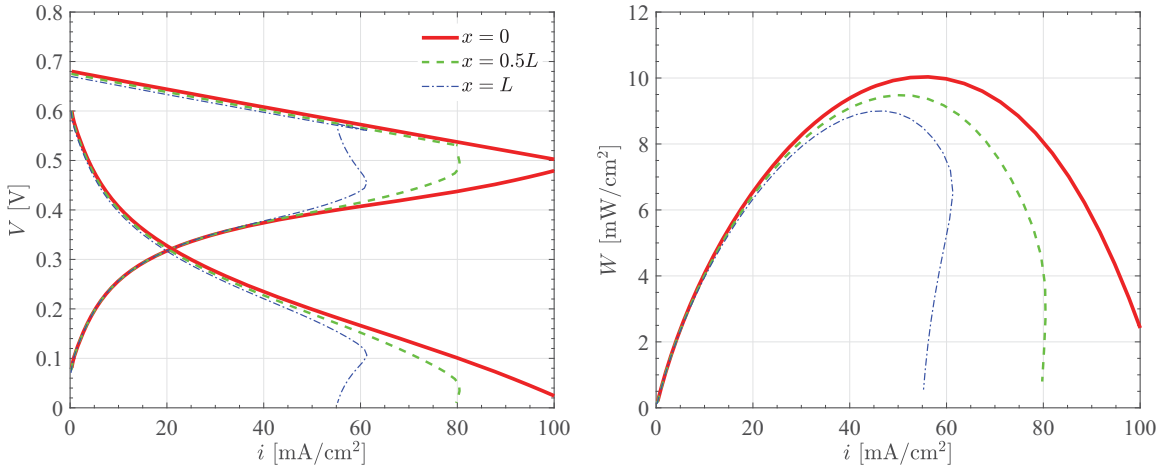

Figure 6: Polarization and power density curves for the 25 cm^2 cell. Left: cell voltage (solid lines), cathode potential (dashed lines) and anode overpotential (dash-dotted lines) computed with the present model at different sections along the flow channels. Right: power density curves corresponding to the polarization curves shown on the left.

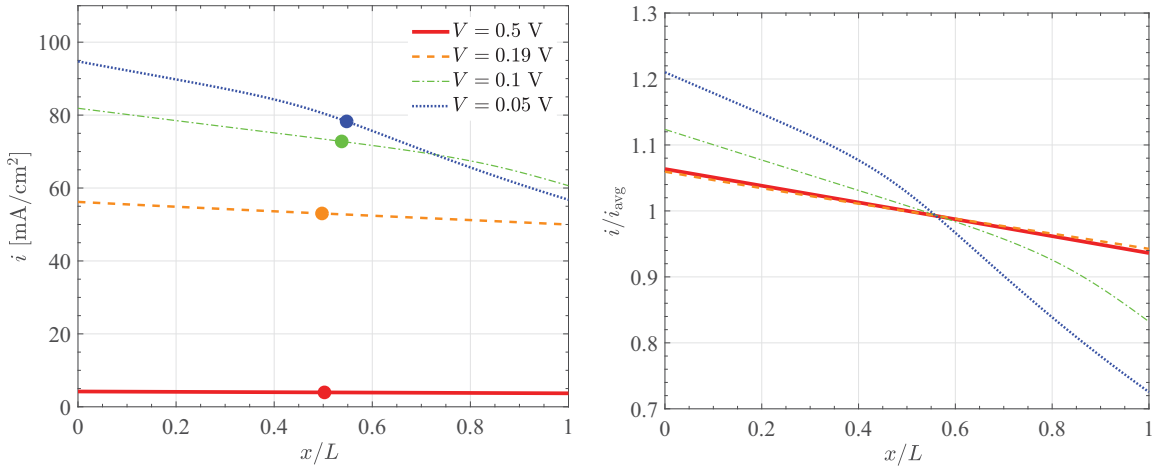

Figure 7: Evolution of the cell current density along the flow channels for different cell voltages. The blue marks indicate the average value of the current density at each cell voltage and the position where it is obtained along the cell. Left: current density. Right: current density measured with the average current density, i_{avg}.

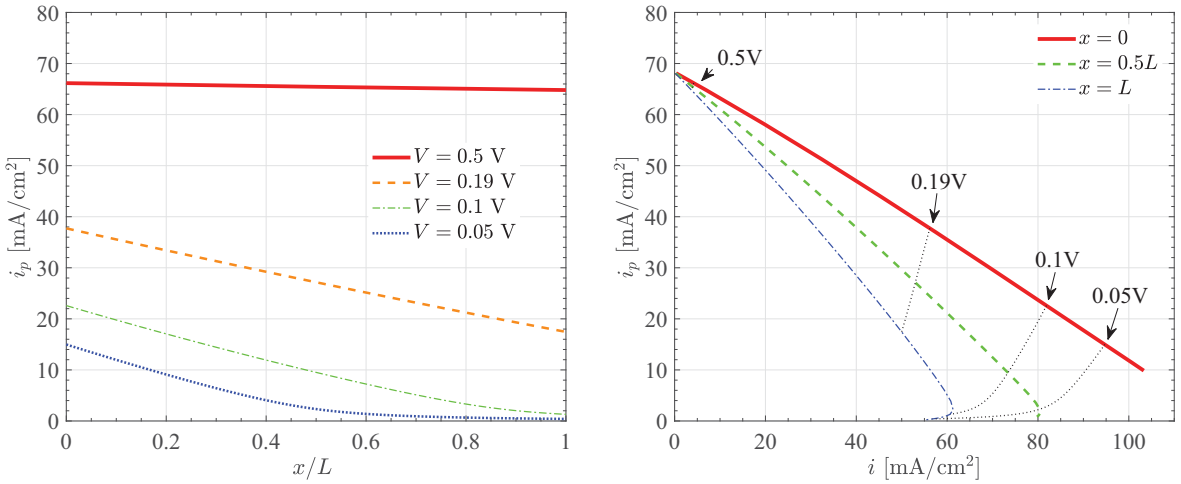

Figure 8: Evolution of the parasitic current density along the flow channels for different cell voltages (left) and variation of the parasitic current density with the cell current density at different sections along the flow channels (right). The dashed lines labeled by arrows correspond to each of the cell voltages represented on the left panel.

Figure 8 shows the variation of the parasitic current density along the flow channel for different cell voltages. In general, the parasitic current density is seen to decay along the channel length due to the reduced availability of ethanol. The variation is steeper at low cell voltages, when reactant consumption is larger. As can be seen, the parasitic current is drastically reduced at very low cell voltages due to reactant starvation. The right panel of Fig. 8 shows the variation of the parasitic current density with the cell current density at different sections along the flow channel. The figure shows that the parasitic current decreases almost linearly with the cell current density, with a slope that becomes more and more negative towards the end of the cell.

As previously discussed, in DEFCs the classical fuel utilization frequently used to characterize DMFC performance should be conveniently replaced by an energy utilization factor ϵ_{U} that includes both the energy content of ethanol and of acetaldehyde, a product of the partial oxidation of ethanol that is still able to be further oxidized releasing additional energy. The energy utilization factor can be defined as follows

$$\epsilon_{\mathrm{U}} = \frac{\Delta H}{\Delta H + \Delta H_{\mathrm{loss}}} \tag{41}$$

where $\Delta H = -(\omega_{\mathrm{E}} \Delta \bar{h}_{\mathrm{E}} + \omega_{\mathrm{A}} \Delta \bar{h}_{\mathrm{A}})$ is the available enthalpy used per unit time to produce current and $\Delta H_{\mathrm{loss}} = -(N_{\mathrm{E,cross}} \Delta \bar{h}_{\mathrm{E}} + N_{\mathrm{A,cross}} \Delta \bar{h}_{\mathrm{A}})$ is the enthalpy loss per unit time due to crossover. Here $\Delta \bar{h}_{\mathrm{E}}$ and $\Delta \bar{h}_{\mathrm{A}}$ are the reaction enthalpies (higher heating values) for the complete oxidation of ethanol and

acetaldehyde at the reference temperature and pressure

$$C_2H_5OH\ (L) + 3O_2 \rightarrow 2CO_2 + 3H_2O\ (L), \qquad \Delta\bar{h}_E = 1367\,kJ/mol \tag{42}$$

$$CH_3CHO\ (L) + \frac{5}{2}O_2 \rightarrow 2CO_2 + 2H_2O\ (L), \qquad \Delta\bar{h}_A = 1167\,kJ/mol \tag{43}$$

Introducing the above expressions for ΔH and ΔH_{loss} in Eq. (41), using Eqs. (A.27) and (A.28) to write $N_k = \omega_k + N_{k,cross}$ in the denominator, with $k = \{E, A\}$, and introducing the ratio $\beta = \Delta\bar{h}_A/\Delta\bar{h}_E \simeq 0.853$, the energy utilization factor can be rewritten as

$$\epsilon_U = \frac{\omega_E + \beta\omega_A}{N_E + \beta N_A} \tag{44}$$

which enables a rapid evaluation of ϵ_U from the local net production (+) or consumption (−) rates of ethanol and acetaldehyde, ω_k, $k = \{E, A\}$, and the net molar fluxes of these species that emerge from (+) or arrive to (−) the anode catalyst layer to/from the anode gas diffusion layer, N_k. Further details on the definition of these variables can be found in the nomenclature, in the Appendix, or elsewhere [66]. It is worth noting that in the absence of acetaldehyde (i.e., under the assumption of complete oxidation of ethanol to CO_2) the above equation reduces to the classical expression for the fuel utilization used in DMFCs in terms of the output and parasitic current densities, $\epsilon_U = \omega_E/(\omega_E + N_{E,cross}) = i/(i + i_p)$.

Figure 9 shows the variation of ϵ_U along the anode channel for different cell voltages. It can be seen that ϵ_U grows along the cell as a result of the reduction of the parasitic current observed in Fig. 8. The right panel of Fig. 9 shows the variation of ϵ_U with the cell current density at different sections along the flow channel. It is seen that ϵ_U grows almost linearly from 0% at open circuit conditions to almost 100% at the highest current densities reached at each channel station. Note that at maximum power density conditions (0.19 V at the channel inlet) the fuel utilization reaches only a moderate 50%.

The variation of the cell current density along the flow channel induces changes in the net chemical production or consumption rates of the different species. Figure 10 shows the spatial evolution of the molar production rates of ethanol, acetaldehyde, acetic acid and carbon dioxide for different cell voltages. As the primary reacting species, ethanol is consumed along the whole channel length, but its consumption rate is seen to decrease along the channel due to ethanol depletion. Acetaldehyde is the only other free reactive species accounted for in the model, but this species can be either produced or consumed depending on the local flow conditions. For medium-to-high voltages (about 0.15 V or higher) there is net acetaldehyde production along the whole channel. However, for lower voltages acetaldehyde is first produced and then consumed, with higher consumption rates reached near the channel exit. The cell consumes acetaldehyde as a means to compensate the low ethanol concentrations existing near the

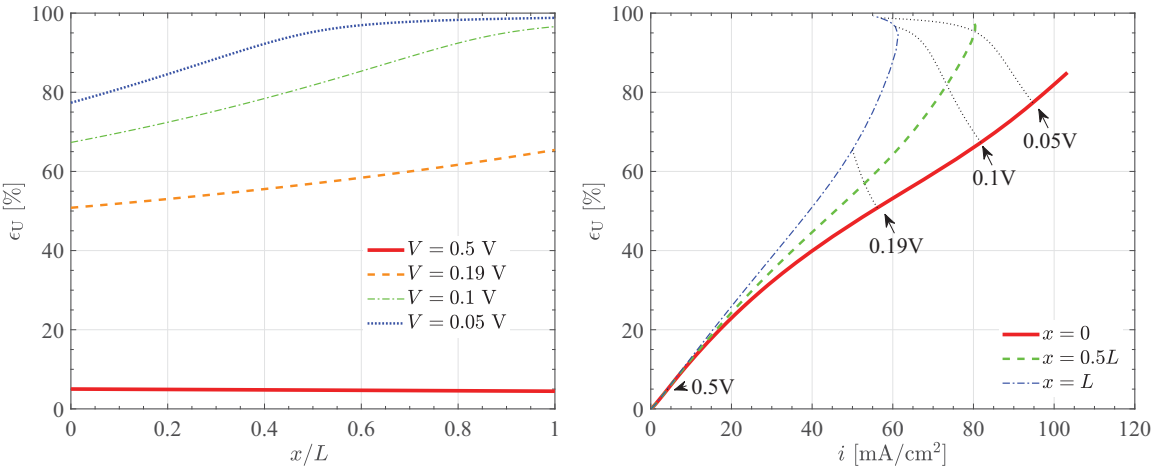

Figure 9: Evolution of the energy utilization along the flow channels for different cell voltages (left) and variation of the fuel utilization with the cell current density at different sections along the flow channel (right). The dashed lines labeled by arrows correspond to each of the cell voltages represented on the left panel.

channel exit as the current density grows more and more. By contrast, the production of acetic acid and CO_2 remains almost constant along the flow channel. Only at very low voltages (ca. $0.1 - 0.05$ V) there is a noticeable reduction of the net production rates of these species. This reduction is associated with the lower availability of ethanol, which can not be fully compensated by acetaldehyde conversion.

Figure 11 shows the variation of the concentrations of ethanol and O_2 at the flow channels and catalyst layers. For the operating conditions under study, corresponding to moderately low anode stoichiometries, a significant reduction of ethanol concentration is observed both at the channel and the catalyst layer except perhaps at the highest voltages, when the cell hardly consumes any ethanol. At maximum power density ($V = 0.19$ V) the ethanol concentration is reduced by a factor of ca. 35% along the flow channel. At the catalyst layer, ethanol starvation is observed at low cell voltages ($V < 0.1$ V) in the downstream part of the channel, coinciding with the conditions leading to the consumption of acetaldehyde.

According to the numerical results, the concentration of oxygen at the cathode catalyst layer does not differ from that at the cathode channel by more than 0.05 mol/m^3. This is a small concentration jump compared to the typical values of C_{O_2} along the cathode channel, ranging between 5 and 10 mol/m^3, which indicates that mass transport looses are small and oxygen is in excess throughout the channel length. Fig. 11b) shows the variation of the oxygen consumption rate along the cathode channel. Note that at the cathode electrode a positive molar flux represents net oxygen consumption. Note also that the oxygen consumption rate varies only slightly in the whole cell voltage range, which results from the large contribution of the parasitic reactions at high voltages. As a result, the oxygen distributions along

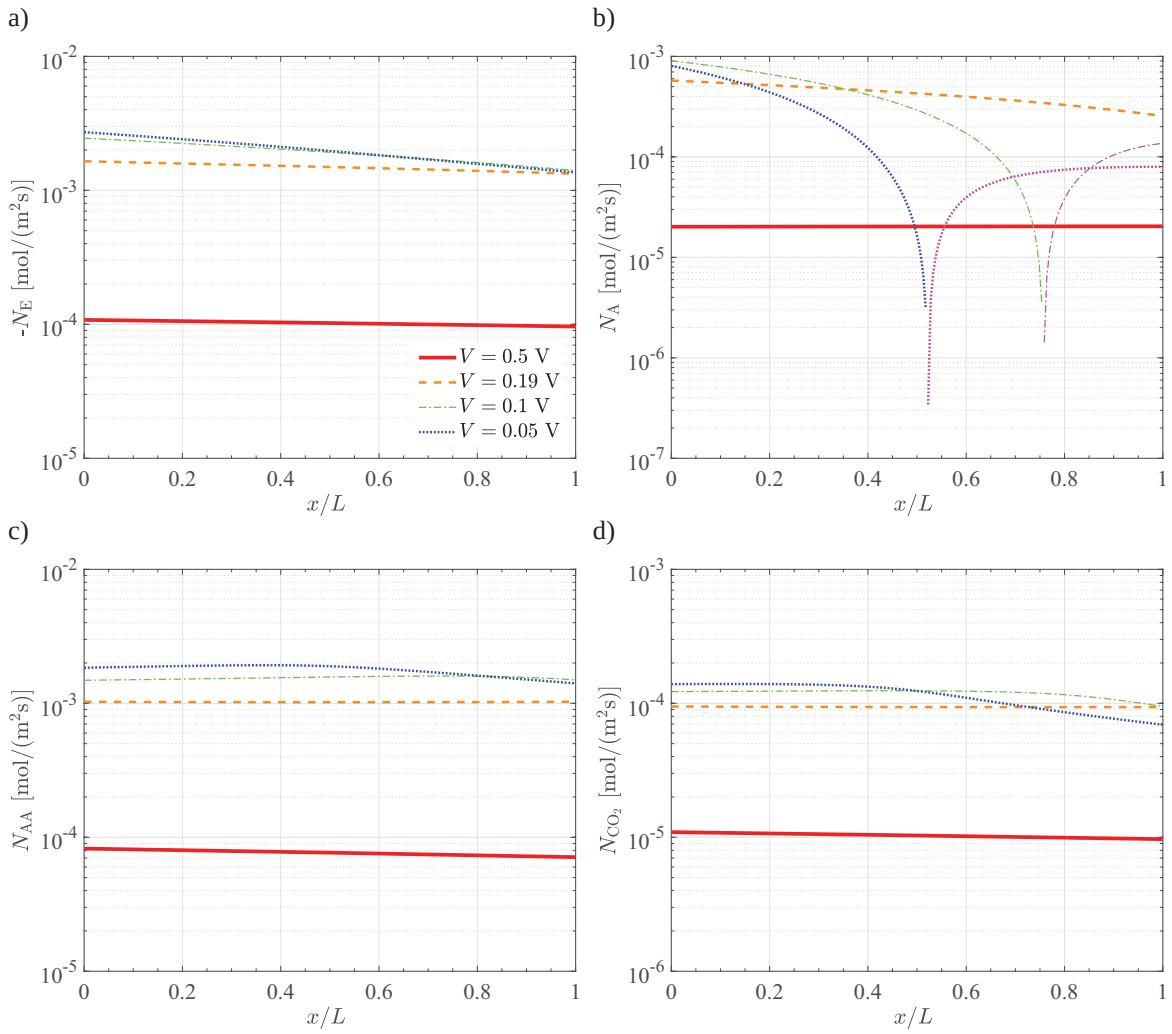

Figure 10: Evolution of the molar production and consumption rates of free species along the anode channel for different cell voltages: a) ethanol (consumption), b) acetaldehyde (first production and later consumption), c) acetic acid (production) and d) CO_2 (production).

the anode channel, shown on the right panel, differ less between high and low voltages than the ethanol distributions shown in Fig. 11a. Note that for the conditions under study the concentration of oxygen at the channel exit decreases to, roughly, half of its initial value for cell voltages below 0.19 V.

The main products of the EOR at the anode electrode are acetaldehyde, acetic acid and CO_2. The concentration of these species along the channel and catalyst layer is shown in Figure 12. As already discussed, acetaldehyde is not strictly a final product, as it can be either produced or consumed to give further products at different points in the cell. As previously discussed, for cell voltages lower than 0.19 V the concentration of acetaldehyde first increases due to the net production rates induced by the

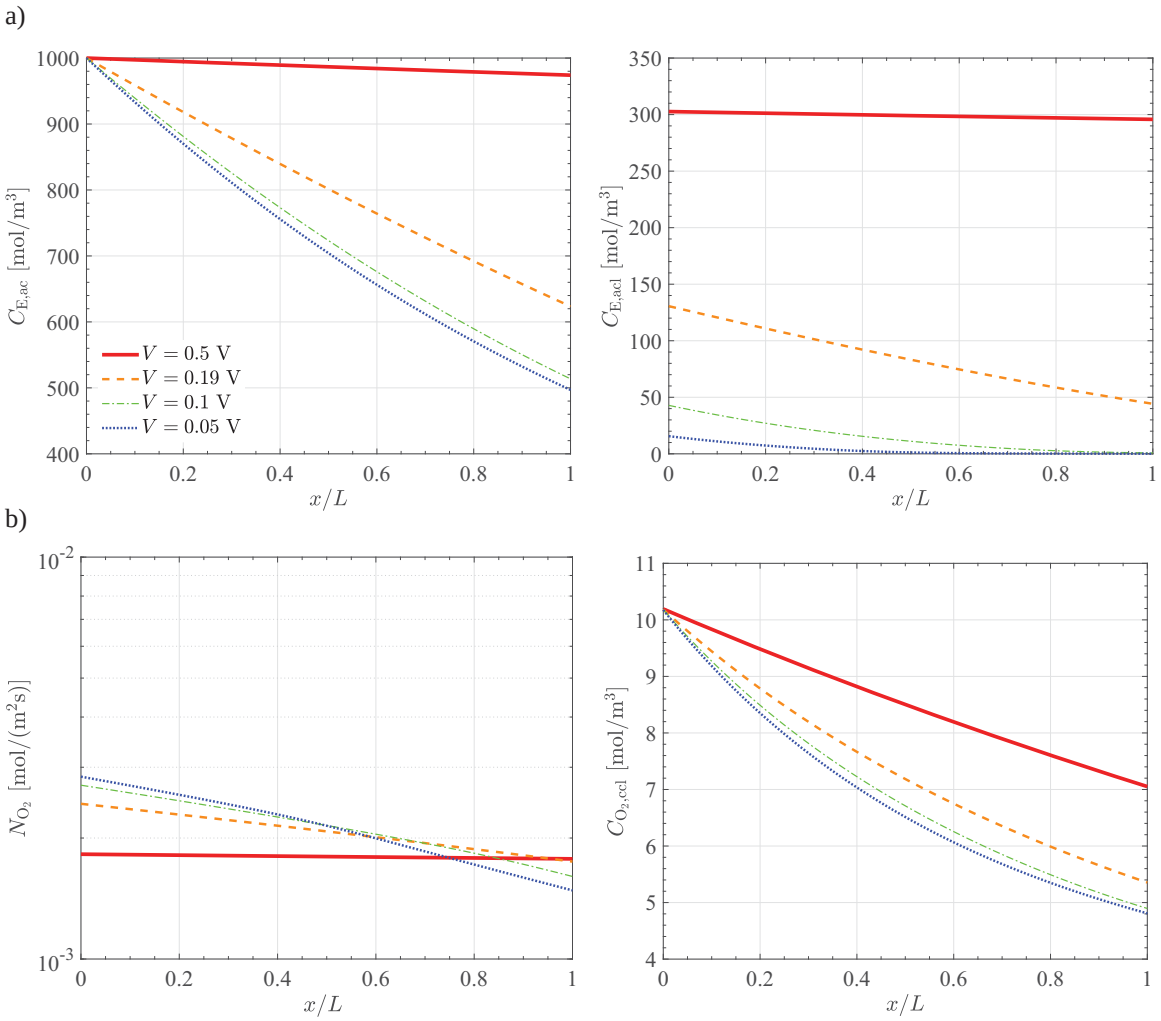

Figure 11: Evolution of a) the molar concentration of ethanol along the anode channel (left) and catalyst layer (right) and b) the molar consumption rate of O_2 along the cathode channel (left) and of the molar concentration of O_2 at the catalyst layer (right).

availability of ethanol, then reaches a peak, and finally decreases towards the channel exit due to the net consumption rates induced by ethanol starvation (see Fig. 10b). However, the consumption of acetaldehyde cannot fully compensate the lack of ethanol, particularly at very low voltages, when acetaldehyde is also starved at the very end of the channel. This, in turn, has a negative impact on CO_2 production, whose concentration at the catalyst layer is also reduced, as can be seen in Fig. 12c.

Fig. 13 shows the evolution of the product selectivities along the channel. To avoid the negative values of the selectivity of acetaldehyde that would result from the application of Eq. (2) under the net acetaldehyde consumption conditions ($\omega_A < 0$) prevailing near the channel exit at low cell voltages ($\omega_A < 0$), an alternative definition of the product selectivity is used here based in the product concentrations in the

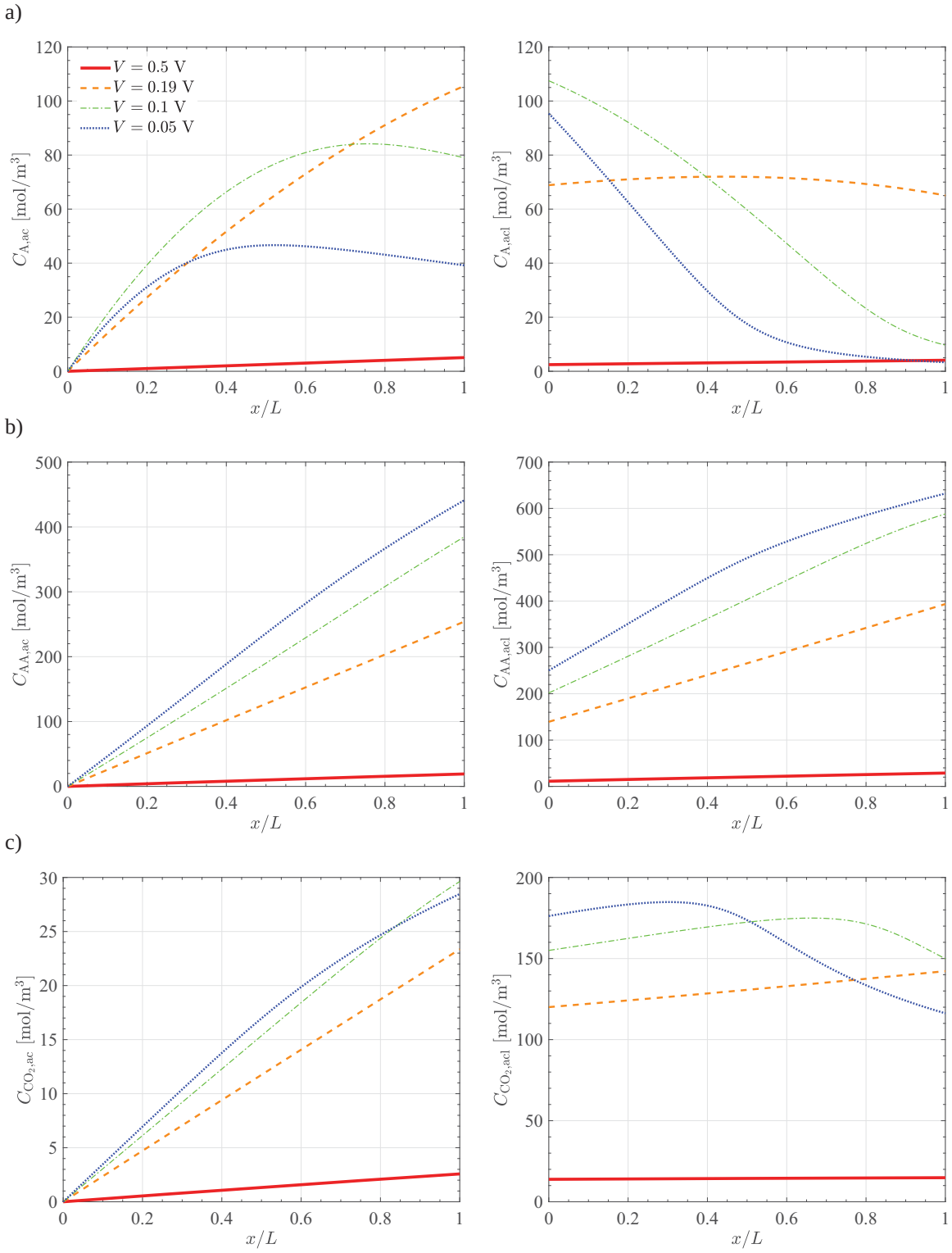

Figure 12: Evolution of the molar concentration of a) acetaldehyde, b) acetic acid and c) CO_2 along the anode channel (left) and at the catalyst layer (right) for different cell voltages.

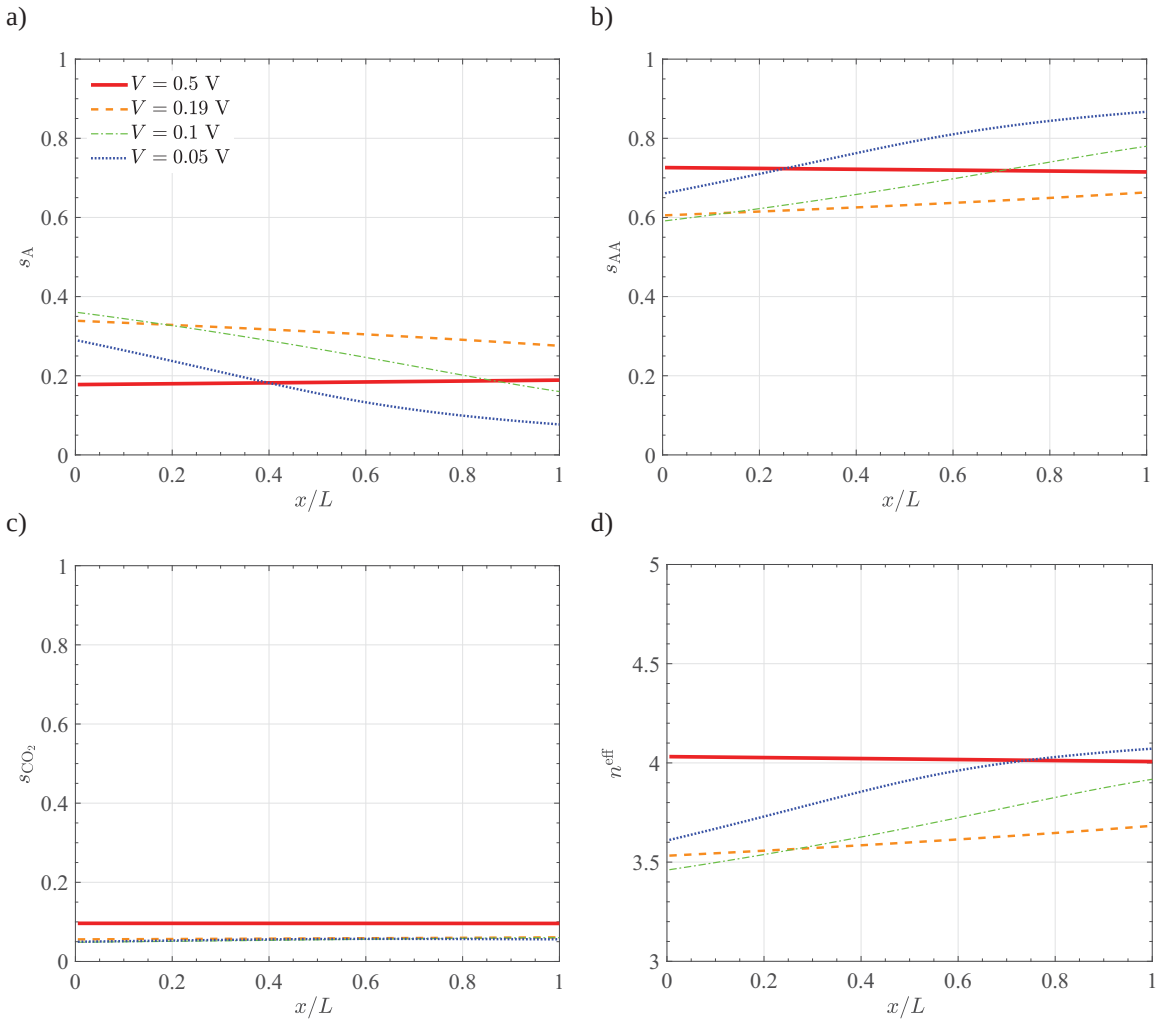

Figure 13: Evolution of the product selectivities of the anode products species along the channel for different cell voltages: a) acetaldehyde, b) acetic acid and c) CO_2. d) shows the evolution of the average number of electrons transferred per ethanol molecule.

anode channel, namely

$$s_k = \frac{C_{k,\mathrm{ac}}}{C_{\mathrm{A,ac}} + C_{\mathrm{AA,ac}} + C_{\mathrm{CO_2,ac}}} \qquad k = \mathrm{A, AA, CO_2} \tag{45}$$

where the small effect of methane production has been neglected, as previously discussed. With this definition, the product selectivities do not truly show local effects, but result from the integrated production of a given species from the cell inlet up to a certain downstream location along the channel. Similarly, the average number of electrons per ethanol molecule computed from the channel concentration selectivities

$$n^{\mathrm{eff}} = \frac{2s_{\mathrm{A}} + 4s_{\mathrm{AA}} + 6s_{\mathrm{CO_2}}}{1 - \frac{1}{2}s_{\mathrm{CO_2}}} \tag{46}$$

represents not a local value but one resulting from the integrated effect of ethanol electro-oxidation from the channel inlet to the specified channel section.

According to Fig. 13 the consumption of acetaldehyde at low cell voltages reduces the selectivity of acetaldehyde in favor of acetic acid towards the end of the channel. COD selectivity remains close to 10% in the whole cell voltage range, remaining roughly constant along the channel. And the average number of electrons transferred per ethanol molecule varies between 3.5 an 4 in agreement with the values reported in [66], with the reduction of ethanol concentration along the flow channel being responsible of the increased number of electrons released per ethanol molecule as a result of the increased selectivity of acetic acid under ethanol starvation conditions.

6.2. Effect of anode flow rate and ethanol feed concentration

This section presents a parametric study that aims to investigate the effect of the anode flow rate and ethanol feed concentration on DEFC performance. The same 25 cm^2 cell used in the previous section was simulated here with different anode flow rates $Q_{ac,in} = \{5, 1, 0.5, 0.1\}$ ml/min and ethanol feed concentrations $C_{E,in} = \{2, 1, 0.5, 0.2\}$ M. Tables 4 and 3 summarize the remaining design and operational parameters, which are kept unchanged in this study.

Figure 14 shows cell voltage, power density, parasitic current and fuel utilization vs. current density curves for the whole range of operational parameters under study. High ethanol feed concentrations induce increased crossover rates and therefore higher parasitic current densities. Consequently, when the cell is operated at 2M ethanol feed concentration fuel utilization barely reaches 50%. This effect reduces the cell performance in the whole operational range, although it also lessens ethanol starvation at low cell potentials thus increasing the limiting current density. Maximum power density is reached with 0.5M ethanol feed concentration, but 1M reaches almost the same peak but with a much larger limiting current density, which guarantees a more stable cell operation. This value is similar to other optimum feed concentrations reported in the literature [50, 55, 70, 75, 81] what makes us gain confidence in the results of the model. It is also seen that reduced ethanol feed concentrations lead to high fuel utilizations, ca. 100%, due to the reduced crossover rates.

Figure 15 shows the concentrations of ethanol, acetaldehyde, acetic acid and CO_2 at the anode outlet. The concentration of ethanol decreases almost linearly with the cell current density, the slope of the curve being steeper as the anode flow rate is reduced. The concentration of acetaldehyde increases with the cell current density until ethanol starvation is reached, when it starts to decline. For low ethanol feed molarity (below, say, 0.5M) the concentration of acetaldehyde at the outlet vanishes at low cell potentials, meaning that it is completely depleted before leaving the cell. Figure 16 shows this same effect in terms of the

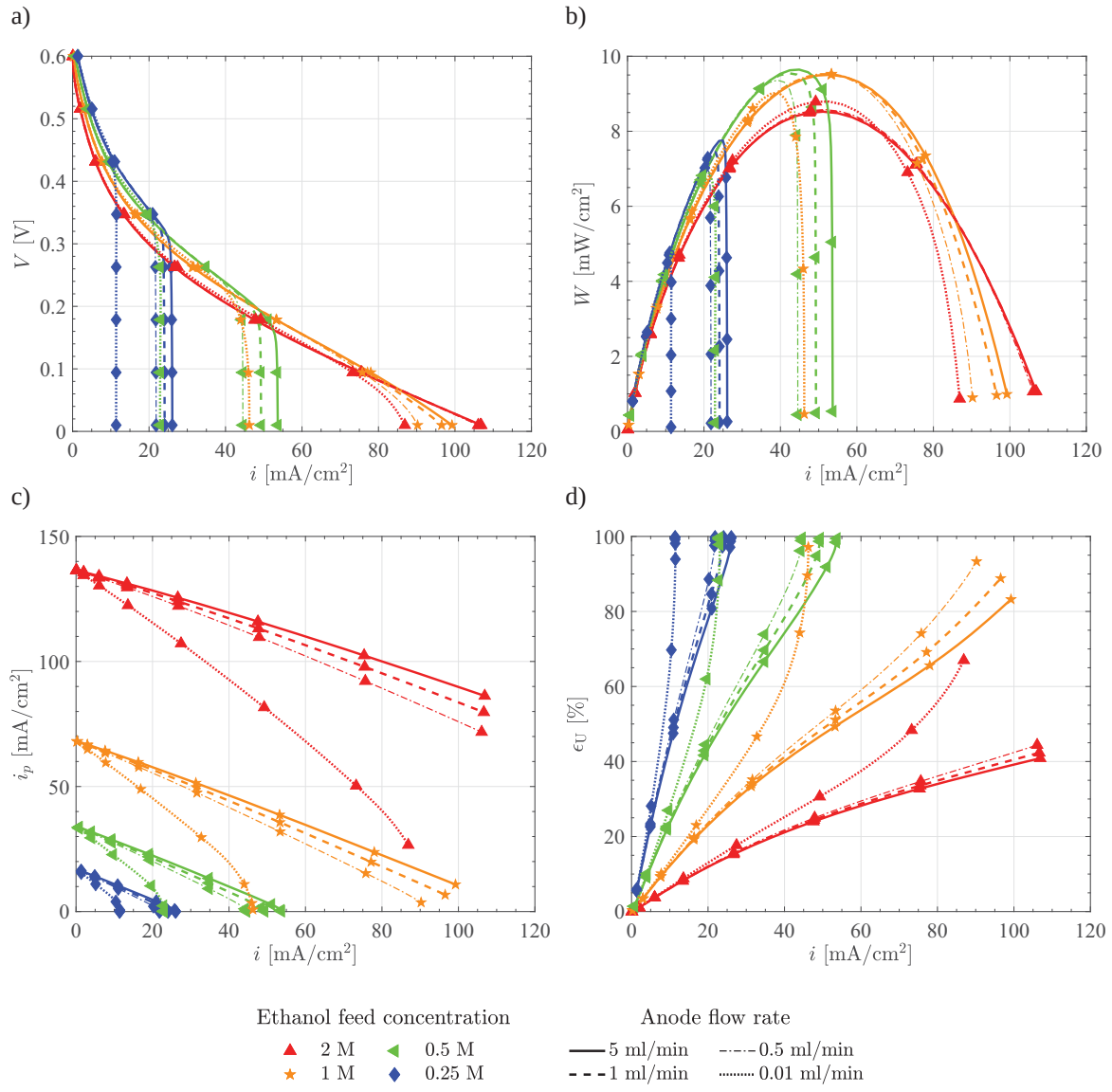

Figure 14: Overall cell performance computed with the present model for the different anode flow rates and ethanol feed concentrations indicated in the legend: a) cell voltage, b) power density, c) average parasitic current density and d) average fuel utilization as a function of the average cell current density. Other design and operational parameters as specified in Tables 4 and 3.

average molar production rates. It is seen that acetaldehyde production peaks and ethanol consumption declines as the cell current density is increased, particularly when ethanol starvation starts to affect EOR kinetics.

In the case of acetic acid, both the outlet concentration (Fig. 15c) and the molar production rate (Fig. 16c) increase steadily with the current density, exhibiting a sharper growth rate under ethanol starvation

conditions. The outlet concentration of CO_2 grows with the current density but remains significantly lower than those of acetaldehyde and acetic acid due to its lower selectivity. Figures 15 and 16 also show that at low ethanol feed concentrations (below 0.5M) the outlet concentration and net production rate of CO_2 are sharply reduced. This is a result of the enhanced production of acetic acid discussed before under ethanol starvation conditions. The reduction of CO_2 production in this regime is due to the presence of oxidants such OH_{ads} [11], which favors the production of acetic acid at the expense of the C-C bond breaking steps (Reactions 4 and 5, respectively, in Table 1). A closer analysis of the values of the reaction constants shown in Table 1 reveals that k_4 is almost two orders of magnitude larger than k_5. Thus, as soon as the coverage factor of the adsorbed hydroxyl group becomes significant, which occurs at high anode overpotentials, Reaction 4 becomes dominant thus hindering the further production of CO_2.

Figure 17 shows the product selectivities at the anode outlet as a function of the cell current density. The overall behavior resembles that discussed in our previous work [66], but appropriately rescaled here with the limiting current density, which depends both on the anode flow rate and the ethanol feed concentration. Acetaldehyde selectivity decreases as the limiting current is reduced, until it vanishes under severe starvation conditions. Under these conditions, acetic acid selectivity grows sharply beyond 0.8, reaching 0.95 for the lowest ethanol molarities. Simultaneously, CO_2 selectivity drops to roughly 0.05. The reduction in acetaldehyde selectivity increases the average number of electrons transferred per ethanol molecule, which grows beyond 4 under severe starvation conditions due to the importance of acetic acid production. Note again that the highest values of n^{eff} are reached for the lowest acetaldehyde selectivities, indicating a better utilization of the ethanol consumed. Thus, for 1M ethanol feed the value of n^{eff} is about 0.5 larger than for 2M at high current densities (> 70 mA/cm^2), implying a more efficient cell operation.

As previously discussed, the results presented so far enable the calculation of the overall efficiency of the cell using Eq. (1). The computed cell efficiency is shown in Figure 18 as a function of the output current density. The curves were obtained by computing separately the theoretical, voltage, faradaic and energy utilization efficiencies and multiplying them to get the value of ϵ_T. In general trends, DEFC efficiency increases for decreasing ethanol mass flow rate, with ethanol molarity having a greater impact than the anode flow rate. As can be seen, the cell efficiency ranges from 1% for the highest molarity (2M) to 8-10% for the lowest ethanol molarity (0.25M), indicating that the fuel conversion efficiency of the cell under study is quite poor. Clearly, the fuel cell fixture used by Li & Pickup [74] was not optimized for cell efficiency, but to demonstrate the ability to separate the cell performance losses into the cathode and anode electrodes. This in turn was crucial for the setup of the detailed EOR kinetic

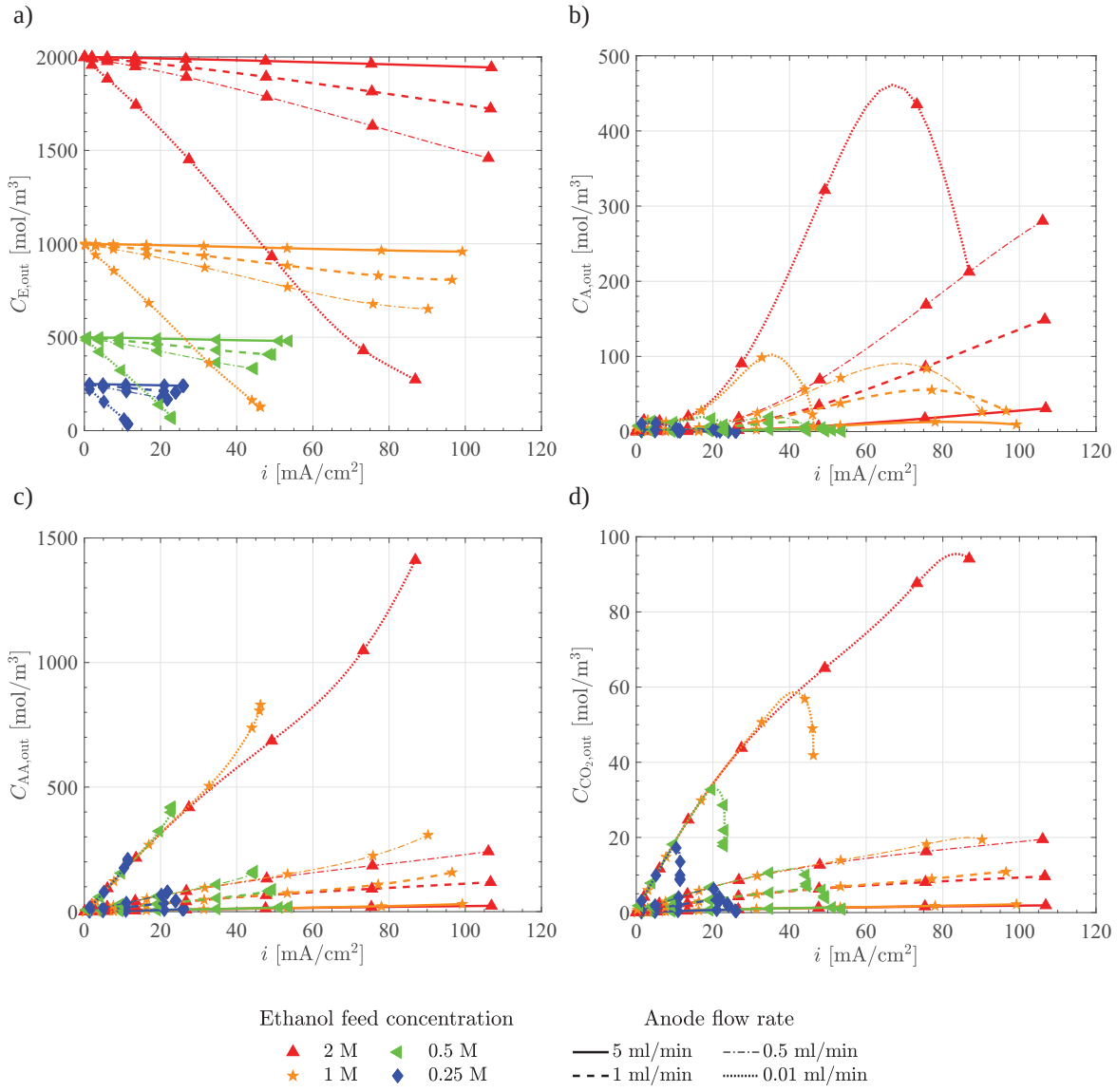

Figure 15: Species concentrations at the anode channel outlet for the different anode flow rates and ethanol feed concentrations indicated in the legend: a) ethanol, b) acetaldehyde, c) acetic acid and d) CO_2 obtained with the model presented in this thesis. Other design and operational parameters as specified in Tables 4 and 3.

model used in this work [66]. The combination of advanced experimental diagnostic tools with next-generation mathematical models such as the one proposed here would surely provide further insight in the performance and efficiency losses of state-of-the-art and future DEFCs, which should reach much higher overall efficiencies than the ones reported here for the commercial success of this technology.

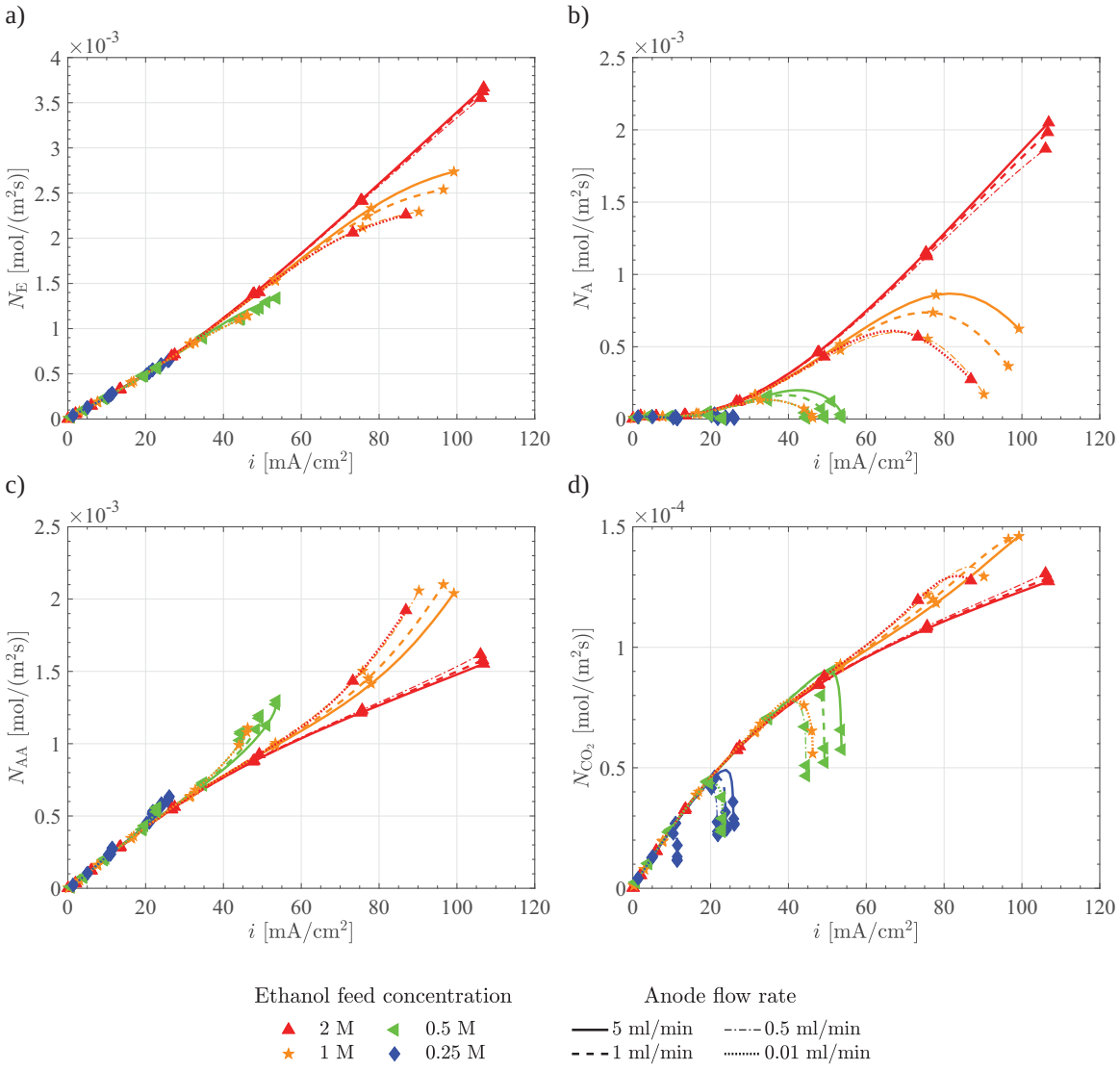

Figure 16: Average molar consumptions/production rates at the anode for the different flow rates and ethanol feed concentrations indicated in the legend: a) ethanol (consumption), b) acetaldehyde (production), c) acetic acid (production) and d) CO_2 (production). Other design and operational parameters as specified in Tables 4 and 3.

7. Conclusions

A 1D+1D model for direct ethanol fuel cells that includes a detailed kinetic description of the anodic ethanol oxidation reaction has been presented and discussed. Following our recent work [66], the rates of the elementary reactions are described by Butler-Volmer kinetics and are coupled to a 1D across-the-channel mass transport model that incorporates the effect of ethanol and acetaldehyde crossover. A simple diffusive model with overall Butler-Volmer kinetics for the oxygen reduction reaction has been

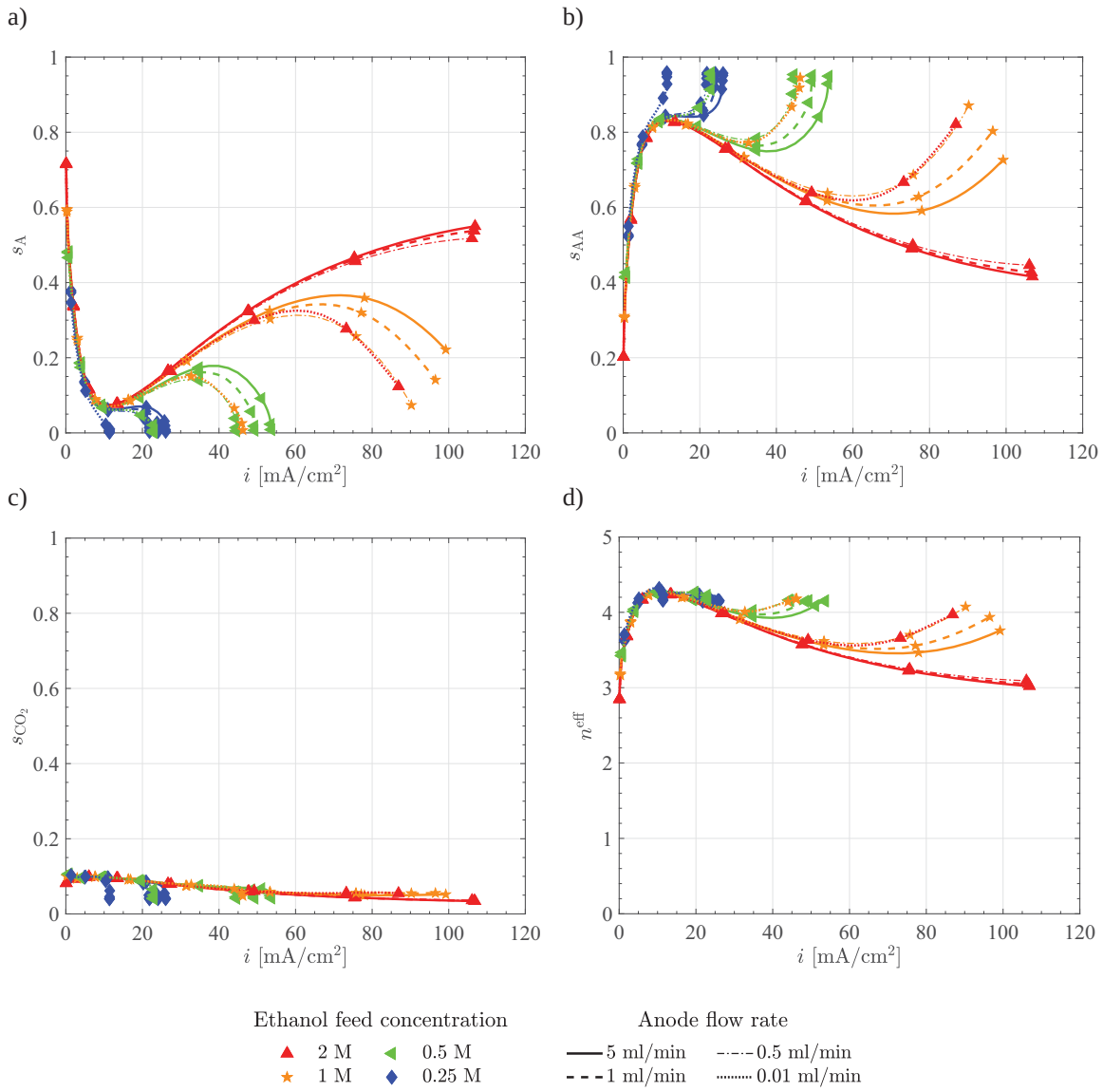

Figure 17: Variation with the current density of a) acetaldehyde, b) acetic acid, and c) CO_2 selectivity, and d) the average number of electrons transferred per ethanol molecule for the different flow rates and ethanol feed concentrations indicated in the legend. Other design and operational parameters as specified in Tables 4 and 3.

added in this work to describe the cathode electrode. The resulting 1D across-the-channel model has been coupled to a 1D along-the-channel advection model to describe the evolution of the different variables of interest along the flow channels, including reactant concentrations at the channels and catalyst layers, molar consumption/production rates, cell overpotentials, output current and parasitic current density. A genetic optimization strategy has been used to determine the effective cathodic exchange current density and the cell electronic/contact resistance that provide a better fit to experimental results taken from the

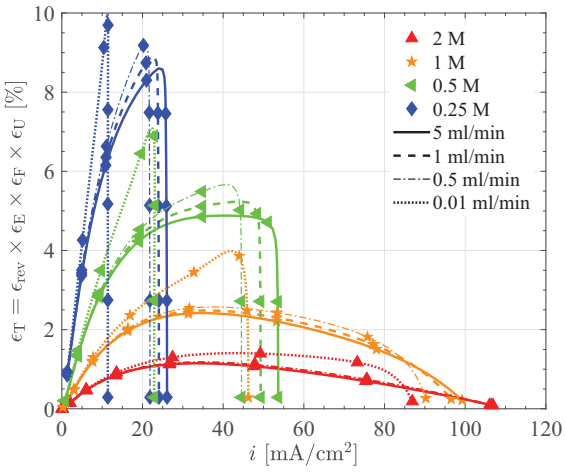

Figure 18: Variation with the current density of the overall cell efficiency for the different anode flow rates and ethanol feed concentrations considered in the parametric study. Other design and operational parameters as specified in Tables 4 and 3.

literature. The effective cathodic exchange current density, which includes here the blocking effect due to poisoning by adsorbates and the presence of liquid water, is much smaller than the typical values reported in the polymer electrolyte membrane fuel cell literature. This results in a severe performance drop in direct ethanol fuel cells due to the reduction of the active catalyst area and the resulting growth of the cathode mixed-overpotential. An extension of the current analysis employing a detailed kinetic mechanism also for the cathode electrode may shed further light on this interesting topic [82].

The analysis shows that ethanol and acetaldehyde are the main species involved in the generation of current at the anode electrode. The evolution of their concentrations along the anode channel affects the ethanol oxidation reaction by changing the local conditions at each channel section. The role of acetaldehyde as the main free intermediate is particularly interesting. Acetaldehyde produced upstream is transported by diffusion to the anode channel and then convected downstream. The acetaldehyde accumulated in the channel can be consumed downstream under ethanol starvation conditions, leading to the existence of a peak acetaldehyde concentration inside the cell that may not be detected at the outlet. Indeed, numerical simulations have shown that under extreme starvation conditions acetaldehyde may be completely depleted before leaving the cell. Under these conditions the cell reaches a high faradaic efficiency for ethanol conversion, although catalysts with enhanced CO_2 selectivity could boost the cell efficiency even further.

After analyzing the downstream evolution along the cell, a parametric study was carried out to asses the effect of different ethanol feed concentrations and anode flow rates on the overall cell performance.

For the conditions under study, the results show the existence of an optimum ethanol feed concentration around 1M for various reasons: 1M exhibits a high maximum power density, a much larger limiting current density that 0.5M, a fuel utilization ca. 70% for high current densities and an average number of electrons transferred per ethanol molecule ca. 4. In terms of cell efficiency, however, lower cell molarity seems to be preferable, although it would limit the output performance. The detailed kinetic description of the ethanol oxidation reaction has enabled the computation of the theoretical, voltage, faradaic end energy utilization efficiencies characterizing the operation of direct ethanol fuel cells, which once combined have led to curves of overall fuel efficiency vs. cell current density that could not have been computed with any other previous DEFC model.

It must be emphasized that the main contribution of this work is not to present a closed model that serves for all DEFCs, but to introduce a fundamental modeling methodology. Trying to adjust a single model to results obtained in DEFCs with different catalysts is simply impossible, due to the large differences in catalytic activities and product selectivities shown by different catalyst compositions, as emphasized in the literature review. As a result, the proposed model (and in fact any other well established DEFC model) should preferably be used in general scenarios in order to identify critical factors that affect the performance of DEFCs, complementing the research carried out experimentally. This is a valuable information for complex systems such as DEFCs, and may contribute to shed light on the different factors limiting the performance of particular cell set-ups.

Acknowledgments

This work has been supported by Project ENE2015-68703-C2-1-R (MINECO/FEDER, UE). P.A. García-Salaberri also thanks the support from the research grant "Ayudas a la Investigación en Energía y Medio Ambiente" of the Spanish Iberdrola Foundation.

Nomenclature

Symbols

$C_{k,\ell}$	molar concentration of species k in layer ℓ [mol m^{-3}]
$D_{k,\ell}$	molecular diffusivity of species k in layer ℓ [m^2 s^{-1}]
F	Faraday's constant, 96487 [C mol^{-1}]
h	mass transport coefficient ac/agdl [m s^{-1}]
i	current density [A m^{-2}]
k_r	rate constant of Reaction r [mol m^{-3} s^{-1}] or [s^{-1}]
n^{eff}	average number of electrons transferred per ethanol molecule
n_d^k	electroosmotic drag coefficient of species k
N_k	molar flux of species k [mol m^{-2} s^{-1}]
q_r	net reaction rate of Reaction r [mol m^{-3} s^{-1}]
R	ideal-gas constant, 8.3143 [J mol^{-1} K^{-1}]
s_k	selectivity of product species k
s^{GRj}	selectivity of global reaction GRj
T	Temperature [K]
v_{W}	drag velocity of water in the anode gdl [m s−1]
W	molar mass [kg mol^{-1}]
y	coordinate across the membrane

Greek letters

α_r	charge transfer coefficient of Reaction r [-]
δ_ℓ	thickness of layer ℓ [μ m]
ϵ	gdl porosity [-]
η	overpotential [V]
Θ_k	coverage factor of adsorbed species k [-]
ρ	fluid density [kg m^{-3}]
ω_k	net molar production rate of free species k [mol m^{-2} s^{-1}]

Subscripts

a	anode
ac	anode channel

acl	anode catalyst layer
agdl	anode gas diffusion layer
ads	adsorbed
A	acetaldehyde (CH_3CHO)
AA	acetic acid (CH_3COOH)
ccl	cathode catalyst layer
cross	crossover flux
E	ethanol (CH_3CH_2OH)
k	species k
ℓ	generic layer
r	reaction r
W	water (H_2O)

Superscripts

eff	effective property

References

[1] Y. Wang, K. S. Chen, J. Mishler, S. C. Cho, X. C. Adroher, A review of polymer electrolyte membrane fuel cells: Technology, applications, and needs on fundamental research, Appl. Energ. 88 (4) (2011) 981–1007. doi:10.1016/j.apenergy.2010.09.030.

[2] Z. Zakaria, S. K. Kamarudin, S. N. Timmiati, Membranes for direct ethanol fuel cells: an overview, Appl. Energ. 163 (2016) 334–342. doi:10.1016/j.apenergy.2015.10.124.

[3] S. P. S. Badwal, S. Giddey, A. Kulkarni, J. Goel, S. Basu, Direct ethanol fuel cells for transport and stationary applications-A comprehensive review, Appl. Energ. 145 (2015) 80–103. doi:10.1016/j.apenergy.2015.02.002.

[4] A. M. Pinto, V. S. Oliveira, D. S. C. Falcao, Direct Alcohol Fuel Cells for Portable Applications: Fundamentals, Engineering and Advances, 1st Edition, Academic Press, 2018.

[5] U. B. Demirci, Direct liquid-feed fuel cells: Thermodynamic and environmental concerns, J. Power Sources 169 (2) (2007) 239–246. doi:10.1016/j.jpowsour.2007.03.050.

[6] J. G. G. Jonker, H. M. Junginger, J. A. Verstegen, T. Lin, L. F. Rodríguez, K. C. Ting, A. P. C. Faaij, F. van der Hilst, Supply chain optimization of sugarcane first generation and eucalyptus second generation ethanol production in brazil, Appl. Energ. 173 (1) (2016) 494–510. doi:10.1016/j.apenergy.2016.04.069.

[7] C. Lamy, A. Lima, V. LeRhun, F. Delime, C. Coutanceau, J.-M. Léger, Recent advances in the development of direct alcohol fuel cells (DAFC), J. Power Sources 105 (2) (2002) 283–296. doi:10.1016/S0378-7753(01)00954-5.

[8] W. O. Silva, A. C. Queiroz, V. A. Paganin, F. H. B. Lima, Faradaic efficiency of ethanol oxidation to CO2 at metallic nanoparticle/short-side-chain PFSA solid-state electrolyte interfaces investigated by on-line DEMS, J. Electroanal. Chem. 824 (2018) 99–107. doi:10.1016/j.jelechem.2018.07.035.

[9] S. C. Lai, S. E. Kleijn, F. T. Öztürk, V. C. van Rees Vellinga, J. Koning, P. Rodriguez, M. T. Koper, Effects of electrolyte pH and composition on the ethanol electro-oxidation reaction, Catal. Today 154 (1-2) (2010) 92–104. doi:10.1016/j.cattod.2010.01.060.

[10] Y. Wang, S. Zou, W. B. Cai, Recent advances on electro-oxidation of ethanol on Pt-and Pd-based catalysts: From reaction mechanisms to catalytic materials, Catalysts 5 (3) (2015) 1507–1534. doi:10.3390/catal5031507.

[11] R. Kavanagh, X. M. Cao, W. F. Lin, C. Hardacre, P. Hu, Origin of low CO_2 selectivity on platinum in the direct ethanol fuel cell, Angew. Chem. Int. Ed. Engl. 51 (7) (2012) 1572–5. doi:10.1002/anie.201104990.

[12] F. Vigier, C. Coutanceau, A. Perrard, E. M. Belgsir, C. Lamy, Development of anode catalysts for a direct ethanol fuel cell, J. Appl. Electrochem. 34 (4) (2004) 439–446. doi:10.1023/B:JACH.0000016629.98535.ad.

[13] L. An, T. S. Zhao, Y. S. Li, Carbon-neutral sustainable energy technology: direct ethanol fuel cells, Renew. Sust. Energ. Rev. 50 (2015) 1462–1468. doi:10.1016/j.rser.2015.05.074.

[14] M. A. F. Akhairi, S. K. Kamarudin, Catalysts in direct ethanol fuel cell (DEFC): An overview, Int. J. Hydrogen Energy 41 (7) (2016) 4214–4228. doi:10.1016/j.ijhydene.2015.12.145.

[15] P. Majidi, P. G. Pickup, Determination of the average number of electrons released during the oxidation of ethanol in a direct ethanol fuel cell, Electrochim. Acta 182 (2015) 856–860. doi:10.1016/j.electacta.2015.09.168.

[16] R. M. Altarawneh, P. Majidi, P. G. Pickup, Determination of the efficiency of ethanol oxidation in a proton exchange membrane electrolysis cell, J. Power Sources 351 (2017) 106–114. doi:10.1016/j.jpowsour.2017.03.084.

[17] D. D. James, P. G. Pickup, Measurement of carbon dioxide yields for ethanol oxidation by operation of a direct ethanol fuel cell in crossover mode, Electrochim. Acta 78 (2012) 274–278. doi:10.1016/j.electacta.2012.05.120.

[18] R. M. Altarawneh, P. G. Pickup, Determination of the stoichiometry of ethanol oxidation from the flow rate dependence of the current in a proton exchange membrane electrolysis cell, J. Electrochem. Soc. 165 (7) (2018) F479–F483. doi:10.1149/2.0761807jes.

[19] A. Ghumman, P. G. Pickup, Efficient electrochemical oxidation of ethanol to carbon dioxide in a fuel cell at ambient temperature, J. Power Sources 179 (1) (2008) 280–285. doi:10.1016/j.jpowsour.2007.12.071.

[20] P. Majidi, P. G. Pickup, Improving carbon dioxide yields and cell efficiencies for ethanol oxidation by potential scanning, J. Power Sources 269 (2014) 173–179. doi:10.1016/j.jpowsour.2014.07.002.

[21] P. Majidi, P. G. Pickup, Sinusoidal potential cycling operation of a direct ethanol fuel cell to improving carbon dioxide yields, J. Power Sources 268 (2014) 439–442. doi:10.1016/j.jpowsour.2014.06.075.

[22] A. Ghumman, G. Li, D. V. Bennett, P. G. Pickup, Online analysis of carbon dioxide from a direct ethanol fuel cell, J. Power Sources 194 (1). doi:10.1016/j.jpowsour.2009.05.020.

[23] D. D. James, D. V. Bennett, G. Li, A. Ghumman, R. J. Helleur, P. G. Pickup, Online analysis of products from a direct ethanol fuel cell, Electrochem. Commun. 11 (10) (2009) 1877–1880. doi:10.1016/j.elecom.2009.08.007.

[24] R. M. Altarawneh, T. M. Brueckner, B. Chen, P. G. Pickup, Product distributions and efficiencies for ethanol oxidation at PtNi octahedra, J. Power Sources 400 (2018) 369–376. doi:10.1016/j.jpowsour.2018.08.052.

[25] A. Ghumman, C. Vink, O. Yepez, P. G. Pickup, Continuous monitoring of CO_2 yields from electrochemical oxidation of ethanol: Catalyst, current density and temperature effects, J. Power Sources 177 (1) (2008) 71–76. doi:10.1016/j.jpowsour.2007.11.009.

[26] R. M. Altarawneh, P. G. Pickup, Product distributions and efficiencies for ethanol oxidation in a proton exchange membrane electrolysis cell, J. Electrochem. Soc. 164 (7) (2017) F861–F865. doi:10.1149/2.0051709jes.

[27] R. M. Altarawneh, P. G. Pickup, Pt and PtRu catalyst bilayers increase efficiencies for ethanol oxidation in proton exchange membrane electrolysis and fuel cells, J. Power Sources 366 (2017) 27–32. doi:10.1016/j.jpowsour.2017.09.014.

[28] B. Chen, T. M. Brueckner, R. M. Altarawneh, P. G. Pickup, Composition dependence of ethanol oxidation at ruthenium-tin oxide/carbon supported platinum catalysts, J. Electrochem. Soc. 165 (15) (2018) J3019–J3025. doi:10.1149/2.0041815jes.

[29] D. D. James, R. B. Moghaddam, B. Chen, P. G. Pickup, Ruthenium-tin oxide/carbon supported platinum catalysts for electrochemical oxidation of ethanol in direct ethanol fuel cells, J. Electrochem. Soc. 165 (3) (2018) F215–F219. doi:10.1149/2.1071803jes.

[30] T. M. Brueckner, P. G. Pickup, Kinetics and stoichiometry of methanol and ethanol oxidation in multi-anode proton exchange membrane mells, J. Electrochem. Soc. 164 (12) (2017) F1172–F1178. doi:10.1149/2.1181712jes.

[31] A. Sayadi, P. G. Pickup, Evaluation of ethanol oxidation catalysts by rotating disc voltammetry, Electrochim. Acta 215 (2016) 84–92. doi:10.1016/j.electacta.2016.08.097.

[32] D. D. James, P. G. Pickup, Effects of crossover on product yields measured for direct ethanol fuel cells, Electrochim. Acta 55 (11) (2010) 3824–3829. doi:10.1016/j.electacta.2010.02.007.

[33] C.-Y. Wang, Fundamental models for fuel cell engineering, Chem. Rev. 104 (10) (2004) 4727–4765. doi:10.1021/cr020718s.

[34] A. Z. Weber, R. M. Darling, J. Newman, Modeling two-phase behavior in PEFCs, J. Electrochem. Soc. 151 (10) (2004) A1715–A1727. doi:10.1149/1.1792891.

[35] M. Secanell, K. Karan, A. Suleman, N. Djilali, Multi-variable optimization of PEMFC cathodes using an agglomerate model, Electrochim. Acta 52 (22) (2007) 6318–6337. doi:10.1016/j.electacta.2007.04.028.

[36] K. Jiao, X. Li, Water transport in polymer electrolyte membrane fuel cells, Prog. Energy Combust. Sci. 37 (3) (2011) 221–291. doi:10.1016/j.pecs.2010.06.002.

[37] A. Z. Weber, R. L. Borup, R. M. Darling, P. K. Das, T. J. Dursch, W. Gu, D. Harvey, A. Kusoglu, S. Litster, M. M. Mench, R. Mukundan, J. P. Owejan, J. G. Pharoah, M. Secanell, I. V. Zenyuk, A critical review of modeling transport phenomena in polymer-electrolyte fuel cells, J. Electrochem. Soc. 161 (12) (2014) F1254–F1299. doi:10.1149/2.0751412jes.

[38] A. Casalegno, R. Marchesi, DMFC performance and methanol cross-over: Experimental analysis and model validation, J. Power Sources 185 (1) (2008) 318–330. doi:10.1016/j.jpowsour.2008.06.071.

[39] T. S. Zhao, C. Xu, R. Chen, W. W. Yang, Mass transport phenomena in direct methanol fuel cells, Prog. Energy Combust. Sci. 35 (3) (2009) 275–292. doi:10.1016/j.pecs.2009.01.001.

[40] P. A. García-Salaberri, M. Vera, On the effect of operating conditions in liquid-feed direct methanol fuel cells: A multiphysics modeling approach, Energy 113 (2016) 1265–1287. doi:10.1016/j.energy.2016.07.074.

[41] E. F. Medici, I. V. Zenyuk, D. Y. Parkinson, A. Z. Weber, J. S. Allen, Understanding water transport in polymer electrolyte fuel cells using coupled continuum and pore-network models, Fuel Cells 16 (6) (2016) 725–733. doi:10.1002/fuce.201500213.

[42] M. Aghighi, J. Gostick, Pore network modeling of phase change in PEM fuel cell fibrous cathode, J. Appl. Electrochem. 47 (12) (2017) 1323–1338. doi:10.1007/s10800-017-1126-6.

[43] L. Chen, H. Luan, Y. Feng, C. Song, Y. L. He, W. Q. Tao, Coupling between finite volume method and lattice Boltzmann method and its application to fluid flow and mass transport in proton exchange membrane fuel cell, Int. J. Heat Mass Transf. 55 (13-14) (2012) 3834–3848. doi:10.1016/j.ijheatmasstransfer.2012.02.020.

[44] P. A. García-Salaberri, M. Vera, I. Iglesias, Modeling of the anode of a liquid-feed DMFC: Inhomogeneous compression effects and two-phase transport phenomena, J. Power Sources 246 (2014) 239–252. doi:10.1016/j.jpowsour.2013.06.166.

[45] P. A. García-Salaberri, D. G. Sánchez, P. Boillat, M. Vera, K. A. Friedrich, Hydration and dehydration cycles in polymer electrolyte fuel cells operated with wet anode and dry cathode feed: A neutron imaging and modeling study, J. Power Sources 359 (2017) 634–655. doi:10.1016/j.jpowsour.2017.03.155.

[46] S. Abdullah, S. K. Kamarudin, U. A. Hasran, M. S. Masdar, W. R. W. Daud, Modeling and simulation of a direct ethanol fuel cell: An overview, J. Power Sources 262 (2014) 401–406. doi:10.1016/j.jpowsour.2014.03.105.

[47] G. M. Andreadis, S. Song, P. E. Tsiakaras, Direct ethanol fuel cell anode simulation model, J. Power Sources 157 (2) (2006) 657–665. doi:10.1016/j.jpowsour.2005.12.040.

[48] G. M. Andreadis, P. E. Tsiakaras, Ethanol crossover and direct ethanol PEM fuel cell performance modeling and experimental validation, Chem. Eng. Sci. 61 (22) (2006) 7497–7508. doi:10.1016/j.ces.2006.08.028.

[49] G. M. Andreadis, A. K. M. Podias, P. E. Tsiakaras, The effect of the parasitic current on the Direct Ethanol PEM Fuel Cell operation, J. Power Sources 181 (2) (2008) 214–227. doi:10.1016/j.jpowsour.2008.01.060.

[50] G. M. Andreadis, A. K. M. Podias, P. E. Tsiakaras, A model-based parametric analysis of a direct ethanol polymer electrolyte membrane fuel cell performance, J. Power Sources 194 (1) (2009) 397–407. doi:10.1016/j.jpowsour.2009.04.064.

[51] S. Lin Ee, E. Birgersson, Two-dimensional approximate analytical solutions for the direct liquid fuel cell, J. Electrochem. Soc. 158 (10) (2011) B1224. doi:10.1149/1.3621950.

[52] H. Pramanik, S. Basu, Modeling and experimental validation of overpotentials of a direct ethanol fuel cell, Chem. Eng. Process. Process Intensif. 49 (7) (2010) 635–642. doi:10.1016/j.cep.2009.10.015.

[53] N. Suresh, S. Jayanti, Cross-over and performance modeling of liquid-feed polymer electrolyte membrane direct ethanol fuel cells, Int. J. Hydrogen Energy 36 (22) (2011) 14648–14658. doi:10.1016/j.ijhydene.2011.07.105.

[54] M. Meyer, J. Melke, D. Gerteisen, Modelling and simulation of a direct ethanol fuel cell considering multistep electrochemical reactions, transport processes and mixed potentials, Electrochim. Acta 56 (11) (2011) 4299–4307. doi:10.1016/j.electacta.2011.01.070.

[55] J. Goel, S. Basu, Mathematical modeling and experimental validation of direct ethanol fuel cell, Int. J. Hydrogen Energ. 40 (41) (2015) 14405–14415. doi:10.1016/j.ijhydene.2015.03.082.

[56] V. B. Oliveira, J. P. Pereira, A. M. F. R. Pinto, Modeling of passive direct ethanol fuel cells, Energy 133 (2017) 652–665. doi:10.1016/j.energy.2017.05.152.

[57] A. Verma, S. Basu, Experimental evaluation and mathematical modeling of a direct alkaline fuel cell, J. Power Sources 168 (1) (2007) 200–210. doi:10.1016/j.jpowsour.2007.02.069.

[58] H. Bahrami, A. Faghri, Multi-layer membrane model for mass transport in a direct ethanol fuel cell using an alkaline anion exchange membrane, J. Power Sources 218 (2012) 286–296. doi:10.1016/j.jpowsour.2012.06.057.

[59] L. An, Z. H. Chai, L. Zeng, P. Tan, T. S. Zhao, Mathematical modeling of alkaline direct ethanol fuel cells, Int. J. Hydrogen Energy 38 (32) (2013) 14067–14075. doi:10.1016/j.ijhydene.2013.08.080.

[60] J. Huang, H. Bahrami, A. Faghri, Analysis of a permselective membrane-free alkaline direct ethanol fuel cell, J. Fuel Cell Sci. Tech. 11 (2) (2014) 021009. doi:10.1115/1.4025931.

[61] W. W. Yang, M. Y. Lu, Y. L. He, Performance study of an alkaline direct ethanol fuel cell with a reduced two-dimensional mass transport model, Int. J. Hydrogen Energy 41 (45) (2016) 20693–20708. doi:10.1016/j.ijhydene.2016.07.060.

[62] R. S. Gomes, A. L. De Bortoli, A three-dimensional mathematical model for the anode of a direct ethanol fuel cell, Appl. Energ. 183 (2016) 1292–1301. doi:10.1016/j.apenergy.2016.09.083.

[63] R. S. Gomes, M. M. De Souza, A. L. De Bortoli, Modeling and simulation of a direct ethanol fuel cell considering overpotential losses and variation of principal species concentration, Chem. Eng. Res. Des. 136 (2018) 371–384. doi:10.1016/j.cherd.2018.05.037.

[64] M. M. De Souza, R. S. Gomes, A. L. De Bortoli, A model for direct ethanol fuel cells considering variations in the concentration of the species, Int. J. Hydrogen Energ. 43 (29) (2018) 13475–13488. doi:10.1016/j.ijhydene.2018.05.096.

[65] R. Sousa, D. M. dos Anjos, G. Tremiliosi-Filho, E. R. Gonzalez, C. Coutanceau, E. Sibert, J.-M. Léger, K. B. Kokoh, Modeling and simulation of the anode in direct ethanol fuels cells, J. Power Sources 180 (1) (2008) 283–293. doi:10.1016/j.jpowsour.2008.01.058.

[66] J. Sánchez-Monreal, P. A. García-Salaberri, M. Vera, A genetically optimized kinetic model for ethanol electro-oxidation on Pt-based binary catalysts used in direct ethanol fuel cells, J. Power Sources 363 (2017) 341–355. doi:10.1016/j.jpowsour.2017.07.069.

[67] M. R. Shivhare, C. L. Jackson, K. Scott, E. B. Martin, Simplified model for the direct methanol fuel cell anode, J. Power Sources 173 (1) (2007) 240–248. doi:10.1016/j.jpowsour.2007.05.004.

[68] D. Gerteisen, Transient and steady-state analysis of catalyst poisoning and mixed potential formation in direct methanol fuel cells, J. Power Sources 195 (19) (2010) 6719–6731. doi:10.1016/j.jpowsour.2010.04.004.

[69] I. Sarris, P. Tsiakaras, S. Song, N. Vlachos, A three-dimensional CFD model of direct ethanol fuel cells: Anode flow bed analysis, Solid state ionics 177 (19–25) (2006) 2133–2138. doi:10.1016/j.ssi.2006.02.019.

[70] J. P. Pereira, D. S. Falcão, V. B. Oliveira, A. M. F. R. Pinto, Performance of a passive direct ethanol fuel cell, J. Power Sources 256 (2014) 14–19. doi:10.1016/j.jpowsour.2013.12.036.

[71] J. Sánchez-Monreal, P. A. García-Salaberri, M. Vera, Mathematical modeling of direct ethanol fuel cells using a multi-step chemical kinetic mechanism, ECS Trans. 72 (25) (2016) 1–16. doi:10.1149/07225.0001ecst.

[72] M. Watanabe, S. Motoo, Electrocatalysis by ad-atoms, J. Electroanal. Chem. Interfacial Electrochem. 60 (3) (1975) 275–283. doi:10.1016/S0022-0728(75)80262-2.

[73] F. Vigier, S. Rousseau, C. Coutanceau, J.-M. Leger, C. Lamy, Electrocatalysis for the direct alcohol fuel cell, Top. Catal. 40 (1–4) (2006) 111–121. doi:10.1007/s11244-006-0113-7.

[74] G. Li, P. G. Pickup, Analysis of performance losses of direct ethanol fuel cells with the aid of a reference electrode, J. Power Sources 161 (1) (2006) 256–263. doi:10.1016/j.jpowsour.2006.03.071.

[75] S. Song, W. Zhou, Z. Liang, R. Cai, G. Sun, Q. Xin, V. Stergiopoulos, P. Tsiakaras, The effect of methanol and ethanol cross-over on the performance of PtRu/C-based anode DAFCs, Appl. Catal. B Environ. 55 (1) (2005) 65–72. doi:10.1016/j.apcatb.2004.05.017.

[76] A. Jablonski, P. J. Kulesza, A. Lewera, Oxygen permeation through Nafion 117 membrane and its impact on efficiency of polymer membrane ethanol fuel cell, J. Power Sources 196 (10) (2011) 4714–4718. doi:10.1016/j.jpowsour.2011.01.045.

[77] K. Scott, W. Taama, J. Cruickshank, Performance and modelling of a direct methanol solid polymer electrolyte fuel cell, J. Power Sources 65 (1–2) (1997) 159–171. doi:10.1016/S0378-7753(97)02485-3.

[78] L. M. Pant, A. Z. Weber, Communication–modeling polymer-electrolyte fuel-cell agglomerates with double-trap kinetics, J. Electrochem. Soc. 164 (11) (2017) E3102–E3104. doi:10.1149/2.0111711jes.

[79] D. R. Lide, Handbook of Chemistry and Physics, CRC Press, Boca Raton, 1990.

[80] Z. H. Wang, C. Y. Wang, Mathematical modeling of liquid-feed direct methanol fuel cells, J. Electrochem. Soc. 150 (4) (2003) A508–A519. doi:10.1149/1.1559061.

[81] M. H. M. T. Assumpção, J. Nandenha, G. S. Buzzo, J. C. M. Silva, E. V. Spinacé, A. O. Neto, R. F. B. De Souza, The effect of ethanol concentration on the direct ethanol fuel cell performance and products distribution: A study using a single fuel cell/attenuated total reflectance-Fourier transform infrared spectroscopy, J. Power Sources 253 (2014) 392–396. doi:10.1016/j.jpowsour.2013.12.088.

[82] J. Sánchez-Monreal, M. Vera, P. A. García-Salaberri, Fundamentals of electrochemistry with application to direct alcohol fuel cell modeling, in: Proton Exchange Membrane Fuel Cell, Intech, Rijeka, 2018, pp. 121–154. doi:10.5772/intechopen.71635.

Appendix A. 1D Anode model

This section summarizes the 1D across-the-channel model used for the anode electrode. For further details the reader is referred to [66].

Appendix A.1. Kinetic model

The net reaction rate for the 11 reaction steps, expressed in moles per unit time and per unit volume of anode catalyst layer, are given by

$$q_{\mathrm{I}} = (1 - \Theta_{\mathrm{CH_3CHOH_{ads}}} - \Theta_{\mathrm{CH_3CO_{ads}}} - \Theta_{\mathrm{CO_{ads}}} - \Theta_{\mathrm{CH_{3\,ads}}})\, C_{\mathrm{E,acl}} k_{\mathrm{If}} \exp\left(\frac{\alpha_{\mathrm{I}} F}{RT}\eta_a\right) - \Theta_{\mathrm{CH_3CHOH_{ads}}} k_{\mathrm{Ib}} \exp\left(-\frac{(1-\alpha_{\mathrm{I}})F}{RT}\eta_a\right) \quad \text{(A.1)}$$

$$q_{\mathrm{II}} = \Theta_{\mathrm{CH_3CHOH_{ads}}} k_{\mathrm{II}} \exp\left(\frac{\alpha_{\mathrm{II}} 2F}{RT}\eta_a\right) \quad \text{(A.2)}$$

$$q_{\mathrm{III}} = \Theta_{\mathrm{CH_3CHOH_{ads}}} k_{\mathrm{IIIf}} \exp\left(\frac{\alpha_{\mathrm{III}} F}{RT}\eta_a\right) - (1 - \Theta_{\mathrm{CH_3CHOH_{ads}}} - \Theta_{\mathrm{CH_3CO_{ads}}} - \Theta_{\mathrm{CO_{ads}}} - \Theta_{\mathrm{CH_{3\,ads}}})\, C_{\mathrm{A,acl}} k_{\mathrm{IIIb}} \exp\left(-\frac{(1-\alpha_{\mathrm{III}})2F}{RT}\eta_a\right) \quad \text{(A.3)}$$

$$q_1 = (1 - \Theta_{\mathrm{CH_3CHOH_{ads}}} - \Theta_{\mathrm{CH_3CO_{ads}}} - \Theta_{\mathrm{CO_{ads}}} - \Theta_{\mathrm{CH_{3\,ads}}}) \left[C_{\mathrm{E,acl}} k_{1\mathrm{f}} \exp\left(\frac{\alpha_1 2F}{RT}\eta_a\right) - C_{\mathrm{A,acl}} k_{1\mathrm{b}} \exp\left(-\frac{(1-\alpha_1)2F}{RT}\eta_a\right)\right] \quad \text{(A.4)}$$

$$q_2 = (1 - \Theta_{\mathrm{CH_3CO_{ads}}} - \Theta_{\mathrm{CO_{ads}}} - \Theta_{\mathrm{CH_{3\,ads}}})\, C_{\mathrm{A,acl}} k_{2\mathrm{f}} \exp\left(\frac{\alpha_2 F}{RT}\eta_a\right) - \Theta_{\mathrm{CH_3CO_{ads}}} k_{2\mathrm{b}} \exp\left(-\frac{(1-\alpha_2)F}{RT}\eta_a\right) \quad \text{(A.5)}$$

$$q_3 = k_{3\mathrm{f}} (1 - \Theta_{\mathrm{OH_{ads}}}) \exp\left(\frac{\alpha_3 F}{RT}\eta_a\right) - k_{3\mathrm{b}} \Theta_{\mathrm{OH_{ads}}} \exp\left(-\frac{(1-\alpha_3)F}{RT}\eta_a\right) \quad \text{(A.6)}$$

$$q_4 = k_4 \Theta_{\mathrm{CH_3CO_{ads}}} \Theta_{\mathrm{OH_{ads}}} \quad \text{(A.7)}$$

$$q_5 = k_5 \Theta_{\mathrm{CH_3CO_{ads}}} \quad \text{(A.8)}$$

$$q_6 = k_6 \Theta_{\mathrm{CO_{ads}}} \Theta_{\mathrm{OH_{ads}}} \exp\left(\frac{\alpha_6 F}{RT}\eta_a\right) \quad \text{(A.9)}$$

$$q_7 = k_7 \Theta_{\mathrm{CH_{3\,ads}}} \Theta_{\mathrm{OH_{ads}}}^2 \exp\left(\frac{\alpha_7 5F}{RT}\eta_a\right) \quad \text{(A.10)}$$

$$q_8 = k_8 \Theta_{\mathrm{CH_3\,ads}} \exp\left(-\frac{\alpha_8 F}{RT}\eta_a\right) \tag{A.11}$$

where η_a is the anode overpotential, $C_{\mathrm{k,acl}}$ is the concentration of the free species k in the anode catalyst layer, Θ_j is the coverage factor of the adsorbed species j, and k_r and α_r are the rate constant and charge transfer coefficient of reaction r, with the values given in Table 1.

Applying the steady-state approximation (SSA) to the adsorbed species results in the following set of nonlinear algebraic equations

$$\mathrm{CH_3CHOH_{ads}}: \quad q_{\mathrm{I}} - q_{\mathrm{II}} - q_{\mathrm{III}} = 0 \tag{A.12}$$

$$\mathrm{CH_3CO_{ads}}: \quad q_2 + q_{\mathrm{II}} - q_5 - q_4 = 0 \tag{A.13}$$

$$\mathrm{OH_{ads}}: \quad q_3 - q_4 - q_6 - 2q_7 = 0 \tag{A.14}$$

$$\mathrm{CO_{ads}}: \quad q_5 - q_6 = 0 \tag{A.15}$$

$$\mathrm{CH_{3\,ads}}: \quad q_5 - q_8 - q_7 = 0 \tag{A.16}$$

which provides the coverage factors of the five adsorbates ($\mathrm{CH_3CHOH_{ads}}$, $\mathrm{CH_3CO_{ads}}$, $\mathrm{CO_{ads}}$, $\mathrm{CH_{3\,ads}}$, and $\mathrm{OH_{ads}}$) for specified values of $C_{\mathrm{E,acl}}$, $C_{\mathrm{A,acl}}$, and η_a.

Once the coverage factors are known, the area-specific net production rates of free species, expressed in moles per unit time and per unit surface area of anode catalyst layer, can be written as

$$\omega_{\mathrm{E}} = -(q_{\mathrm{I}} + q_1)\,\delta_{\mathrm{acl}} \tag{A.17}$$

$$\omega_{\mathrm{A}} = (q_1 + q_{\mathrm{III}} - q_2)\,\delta_{\mathrm{acl}} \tag{A.18}$$

$$\omega_{\mathrm{AA}} = q_4 \delta_{\mathrm{acl}} \tag{A.19}$$

$$\omega_{\mathrm{CO_2}} = (q_6 + q_7)\,\delta_{\mathrm{acl}} \tag{A.20}$$

$$\omega_{\mathrm{CH_4}} = q_8 \delta_{\mathrm{acl}} \tag{A.21}$$

$$\omega_{\mathrm{W}} = -q_3 \delta_{\mathrm{acl}} \tag{A.22}$$

with positive (negative) values of ω_k indicating net production (consumption) of species k.

Multiplying the area specific reaction rates, $q_r \delta_{\mathrm{acl}}$, by the number of electrons transferred in each reaction, n_r, summing up all electron generation rates, and multiplying the result by Faraday's constant, gives the current density generated at the anode catalyst layer

$$i = F\,(q_{\mathrm{I}} + 2q_{\mathrm{II}} + q_{\mathrm{III}} + 2q_1 + q_2 + q_3 + q_6 + 5q_7 - q_8)\,\delta_{\mathrm{acl}} \tag{A.23}$$

Appendix A.2. Anode gas diffusion layer

The molar flux of species k transported by convection and diffusion between the bulk fluid in the anode channel (ac) and the anode catalyst layer (acl) is given by

$$N_k\left(C_{k,\mathrm{ac}}; C_{\mathrm{E,acl}}, C_{\mathrm{A,acl}}, \eta_a\right) = -\frac{C_{k,\mathrm{ac}} e^{v_{\mathrm{W}}/k_{k,\mathrm{gdl}}} - C_{k,\mathrm{acl}}}{e^{v_{\mathrm{W}}/k_{k,\mathrm{gdl}}}\left(1 + v_{\mathrm{W}}/h\right) - 1}\, v_{\mathrm{W}} \qquad k = \mathrm{E, A} \tag{A.24}$$

where $k_{k,\mathrm{agdl}} = D^{\mathrm{eff}}_{k,\mathrm{agdl}}/\delta_{\mathrm{acl}}$ is the diffusive mass transfer coefficient of the gas diffusion layer, h is an overall mass transport coefficient in the anode channel, and

$$v_{\mathrm{W}} = \frac{W_{\mathrm{W}}}{\rho_{\mathrm{W}}}\left(\omega_{\mathrm{W}} - n_d^{\mathrm{W}}\frac{i}{F}\right) \tag{A.25}$$

is the drag velocity of water at the anode gas diffusion layer, induced by water consumption at the anodic reaction and the electro-osmotic flux of water across the membrane. Note that the sign of N_k indicates whether the flux is directed in the positive or negative y-direction, whereas the drag velocity of water is always negative, indicating that the flux of water is always in the negative y- direction, i.e., towards the catalyst layer.

Appendix A.3. Ethanol and acetaldehyde crossover

The present model considers the effects of ethanol and acetaldehyde crossover, which are driven by Fickian diffusion and electro-osmotic drag

$$N_{k,\mathrm{cross}}\left(C_{\mathrm{E,acl}}, C_{\mathrm{A,acl}}, \eta_a\right) = -\left[\frac{D^{\mathrm{eff}}_{k,\mathrm{mem}}}{\delta_{\mathrm{mem}}} + \frac{W_{\mathrm{W}}}{\rho_w} n_d^{\mathrm{W}}\frac{i}{F}\right] C_{k,\mathrm{acl}} \qquad k = \mathrm{E, A} \tag{A.26}$$

where W_{W} is the molecular weight of water, ρ_{W} is the density of water, and n_d^{W} is the electroosmotic drag coefficient of water.

Appendix A.4. Determination of the free species concentrations

Mass conservation of ethanol and acetaldehyde establishes that, if the cell operates in steady state, the molar flux of these two species reaching the acl from the agdl must be equal to the net consumption rate plus the corresponding crossover flux

$$N_{\mathrm{E}}\left(C_{\mathrm{E,ac}}; C_{\mathrm{E,acl}}, C_{\mathrm{A,acl}}, \eta_a\right) = \omega_{\mathrm{E}}\left(C_{\mathrm{E,acl}}, C_{\mathrm{A,acl}}, \eta_a\right) + N_{\mathrm{E,cross}}\left(C_{\mathrm{E,acl}}, C_{\mathrm{A,acl}}, \eta_a\right) \tag{A.27}$$

$$N_{\mathrm{A}}\left(C_{\mathrm{A,ac}}; C_{\mathrm{E,acl}}, C_{\mathrm{A,acl}}, \eta_a\right) = \omega_{\mathrm{A}}\left(C_{\mathrm{E,acl}}, C_{\mathrm{A,acl}}, \eta_a\right) + N_{\mathrm{A,cross}}\left(C_{\mathrm{E,acl}}, C_{\mathrm{A,acl}}, \eta_a\right) \tag{A.28}$$

It should be noted that in [66] the + signs in front of the crossover terms were erroneously written as − signs, although all the results were correctly computed because they where obtained from the proper form of the equations given above.

The molar fluxes of the remaining non-adsorbed species (i.e., acetic acid, CO_2, and CH_4) , which do not influence the electro-oxidation rate of ethanol and acetaldehyde, can be obtained *a posteriori* from the corresponding mass balances

$$N_{\mathrm{k}}\left(C_{\mathrm{k,ac}}, C_{\mathrm{k,acl}}; C_{\mathrm{E,acl}}, C_{\mathrm{A,acl}}, \eta_a\right) = \omega_{\mathrm{k}}\left(C_{\mathrm{E,acl}}, C_{\mathrm{A,acl}}, \eta_a\right) \qquad k = \mathrm{AA}, \mathrm{CO_2}, \mathrm{CH_4} \tag{A.29}$$

These are all product species ($\omega_{\mathrm{k}} > 0$) which are not supposed to cross the membrane. As a result, their net molar fluxes are also positive ($N_{\mathrm{k}} > 0$), which indicates a net contribution of these species to the flow in the anode channel.

Appendix A.5. Solution procedure

Given the channel concentrations, $C_{\mathrm{E,ac}}$ and $C_{\mathrm{A,ac}}$, and the anode overpotential, η_a, Eqs. (A.27) and (A.28) constitute a system of two non-linear algebraic equations for the two unknowns $C_{\mathrm{E,acl}}$ and $C_{\mathrm{A,acl}}$. The solution can be obtained numerically using, for instance, the fsolve function in Matlab. This results in an iterative process that involves the repeated solution of the problem (A.12)–(A.16) for the coverage factors for tentative values of $C_{\mathrm{E,acl}}$ and $C_{\mathrm{A,acl}}$. The converged solution provides the local current density, i, the molar fluxes N_k, $k = \mathrm{E}, \mathrm{A}, \mathrm{AA}, \mathrm{CO_2}, \mathrm{CH_4}$, and the drag velocity of water, v_{W}, required as inputs for the downstream evolution of the 1D along-the-channel model.

List of captions for the figures

Figure 1: Schematic representation of the physical domains covered by the one-dimensional across- and along-the-channel models, showing the inlet conditions, the channel and rib dimensions (length, L, channel width, w_{ac}, and rib width, w_{rib}), and the thickness of the different layers of the MEA (δ_ℓ, ℓ = agdl, acl, mem, ccl, cgdl). Left: side view; right: cross-sectional view.

Figure 2: Reaction mechanism for the ethanol oxidation reaction on binary Pt-based catalysts considered in this work. The exact stoichiometries and the values of the kinetic constants are indicated in Table 1.

Figure 3: Schematic representation of the continuity equation and mass conservation equation of species k applied to the n-th channel element. The water velocity v_{W}^n must be used at the anode and the gas velocity v_{g}^n at the cathode.

Figure 4: Left: cell voltage (×), cathode potential (O) and anode overpotential (□) reported by [74] and computed with the present model (solid, dashed and dash-dotted lines, respectively) at different sections along the flow channels as indicated in the legends. Right: computed (solid lines) and experimental (×) power density curves corresponding to the polarization data shown on the left.

Figure 5: Left: cell voltage (×), cathode potential (O) and anode overpotential (□) reported by [54] (symbols) and computed with the present model (lines) for different ethanol feed concentrations.

Figure 6: Polarization and power density curves for the 25 cm^2 cell. Left: cell voltage (solid lines), cathode potential (dashed lines) and anode overpotential (dash-dotted lines) computed with the present model at different sections along the flow channels. Right: power density curves corresponding to the polarization curves shown on the left.

Figure 7: Evolution of the cell current density along the flow channels for different cell voltages. The blue marks indicate the average value of the current density at each cell voltage and the position where it is obtained along the cell. Left: current density. Right: current density measured with the average current density, i_{avg}.

Figure 8: Evolution of the parasitic current density along the flow channels for different cell voltages (left) and variation of the parasitic current density with the cell current density at different sections along the flow channels (right). The dashed lines labeled by arrows correspond to each of the cell voltages represented on the left panel.

Figure 9: Evolution of the energy utilization along the flow channels for different cell voltages (left) and variation of the fuel utilization with the cell current density at different sections along the flow channel (right). The dashed lines labeled by arrows correspond to each of the cell voltages represented on the left panel.

Figure 10: Evolution of the molar production and consumption rates of free species along the anode channel for different cell voltages: a) ethanol (consumption), b) acetaldehyde (first production and later consumption), c) acetic acid (production) and d) CO_2 (production).

Figure 11: Evolution of a) the molar concentration of ethanol along the anode channel (left) and catalyst layer (right) and b) the molar consumption rate of O_2 along the cathode channel (left) and of the molar concentration of O_2 at the catalyst layer (right).

Figure 12: Evolution of the molar concentration of a) acetaldehyde, b) acetic acid and c) CO_2 along the anode channel (left) and at the catalyst layer (right) for different cell voltages.

Figure 13: Evolution of the product selectivities of the anode products species along the channel for different cell voltages: a) acetaldehyde, b) acetic acid and c) CO_2. d) shows the evolution of the average number of electrons transferred per ethanol molecule.

Figure 14: Overall cell performance computed with the present model for the different anode flow rates and ethanol feed concentrations indicated in the legend: a) cell voltage, b) power density, c) average parasitic current density and d) average fuel utilization as a function of the average cell current density. Other design and operational parameters as specified in Tables 4 and 3.

Figure 15: Species concentrations at the anode channel outlet for the different anode flow rates and ethanol feed concentrations indicated in the legend: a) ethanol, b) acetaldehyde, c) acetic acid and d) CO_2 obtained with the model presented in this thesis. Other design and operational parameters as specified in Tables 4 and 3.

Figure 16: Average molar consumptions/production rates at the anode for the different flow rates and ethanol feed concentrations indicated in the legend: a) ethanol (consumption), b) acetaldehyde (production), c) acetic acid (production) and d) CO_2 (production). Other design and operational parameters as specified in Tables 4 and 3.

Figure 17: Variation with the current density of a) acetaldehyde, b) acetic acid, and c) CO_2 selectivity, and d) the average number of electrons transferred per ethanol molecule for the different flow rates and

ethanol feed concentrations indicated in the legend. Other design and operational parameters as specified in Tables 4 and 3.

Figure 18: Variation with the current density of the overall cell efficiency for the different anode flow rates and ethanol feed concentrations considered in the parametric study. Other design and operational parameters as specified in Tables 4 and 3.

List of captions for the tables

Table 1: The 11-step reaction mechanism used in this work [66].

Table 2: Physical constants, convective mass transport coefficient and geometrical parameters used in the 1D across-the-channel model. The fitted parameters $(ai_0)_{c,eff}$ and R_{cont} provided by the optimization algorithm are also shown for reference purposes.

Table 3: Geometrical and operational parameters used in the 1D along-the-channel model.

Table 4: Design and operational parameters used for model fitting and for the parametric study.